



HAL
open science

Investigation techniques and physical aspects of the angle of repose of granular matter

Sacha Duverger, Vasileios Angelidakis, Sadegh Nadimi, Stefano Utili, Stéphane Bonelli, Pierre Philippe, Jérôme Duriez

► **To cite this version:**

Sacha Duverger, Vasileios Angelidakis, Sadegh Nadimi, Stefano Utili, Stéphane Bonelli, et al.. Investigation techniques and physical aspects of the angle of repose of granular matter. *Granular Matter*, 2024, 26 (1), pp.20. 10.1007/s10035-023-01378-z . hal-04222127

HAL Id: hal-04222127

<https://hal.inrae.fr/hal-04222127v1>

Submitted on 28 Sep 2023

HAL is a multi-disciplinary open access archive for the deposit and dissemination of scientific research documents, whether they are published or not. The documents may come from teaching and research institutions in France or abroad, or from public or private research centers.

L'archive ouverte pluridisciplinaire **HAL**, est destinée au dépôt et à la diffusion de documents scientifiques de niveau recherche, publiés ou non, émanant des établissements d'enseignement et de recherche français ou étrangers, des laboratoires publics ou privés.

Investigation techniques and physical aspects of the angle of repose of granular matter

Sacha Duverger¹, Vasileios Angelidakis^{2,3}, Sadegh Nadimi², Stefano Utili², Stéphane Bonelli¹, Pierre Philippe¹ and Jérôme Duriez^{1*}

¹INRAE, Aix Marseille Univ, RECOVER, Aix-en-Provence, France.

²School of Engineering, Newcastle University, Newcastle upon Tyne, United Kingdom.

³Institute for Multiscale Simulation, Friedrich-Alexander-Universität Erlangen-Nürnberg, Germany.

*Corresponding author(s). E-mail(s): jerome.duriez@inrae.fr;

Contributing authors: sacha.duverger@inrae.fr; vasileios.angelidakis@fau.de;
sadegh.nadimi-shahraki@newcastle.ac.uk; stefano.utili@newcastle.ac.uk;
stephane.bonelli@inrae.fr; pierre.philippe@inrae.fr;

Abstract

The repose of granular materials is investigated via two different Discrete Element Method (DEM) implementations in comparison with an experimental reference from a recently proposed benchmark setup. On a methodological standpoint, a rigorous measurement method of the angle of repose (AOR) is first proposed for plane-strain and axisymmetric conditions as encountered in the reference experiments. Additionally, two systematic procedures are designed in order to also determine the void ratio of the heap, as a fundamental property of granular matter possibly influencing the AOR. A physical discussion is then developed on the role of particle shape, considering the non-spherical nature of reference particles with a convexity value of $C = 0.954$. Adopting non-convex multi-spheres aggregates (i.e. clumps), the first DEM modelling approach successfully predicts the AOR within a 8% tolerance. After a convex simplification that neglects local concavities, another approach based on potential particles underestimates to a greater extent the AOR, bringing it down from $35.95 \pm 0.88^\circ$ to $31.26 \pm 0.95^\circ$. For the loading setup(s) at hand, the AOR is eventually shown to bear no constitutive nature. It is for instance independent of initial void ratio but is still different than the critical friction angle. The latter may actually serve as a lower bound for the process-dependent AOR. These conclusions are drawn from a statistical analysis of a large set of results, accounting for the random nature of the microscopic arrangement in the studied process.

Keywords: Angle of repose; Discrete Element Method; Non-spherical particles

1 Introduction

Under loading, particulate matter strains in the form of a fluid-like flow as long as the applied load is high enough. Then, once loading no longer prevails against internal dissipation in terms of energy input, particulate matter comes at rest in a solid-like heap configuration, especially in the absence of cohesion or adhesion. The corresponding slope, expressed in terms of an angle of repose (AOR), rules the spatial extents of the deposit for a given matter quantity. The AOR is therefore of interest for countless applications involving particulate materials, for instance the design of industrial facilities for granular-conveying processes, or the prediction of the coverage of natural deposits after e.g. snow or rock avalanches. Several standardised measurement procedures have been proposed in the literature to measure the AOR of granular materials employing empirical and geometrical concepts [1, 2] but they unfortunately often lead to inconsistent results, as demonstrated in [3], and new measurement devices are still being proposed [4]. As such, an one-to-one correlation of the AOR to theoretically-established mechanical properties is not always demonstrated even though the AOR may be often considered as a material property, e.g. in [5] in geotechnics or in [6, 7] for the purpose of DEM calibration. A part of the complexity certainly stems from an influence of non-constitutive parameters such as the heap construction history

[8] and possible geometrical effects [9, 10]. The latter comes in addition to the more natural influence of physical microscopic properties such as particle shape [11, 12] and contact friction [11, 9, 12], as well as mesoscopic ones, such as fabric [12]. Last, it should be noted that granular heaps may not systematically conform to a linear slope [13, 14] which may prevent one to define a single-valued AOR.

Following up on these previous works, the aim of the present manuscript is twofold. First, rigorous simulation and measurement methods are proposed in order to ease evergoing AOR studies. Second, with the help of these methods, an in-depth study is conducted in order to gain further insights on the AOR variations with respect to physical parameters. The present analysis combines the use of two Discrete Element Method (DEM) approaches and existing experimental results recently proposed by the Japanese Geotechnical Society (JGS) as part of a round robin series of tests [4, 15].

The remainder of the article is as follows. Section 2 first recalls the JGS reference experiments [4] and the two DEM formulations which are both executed within the YADE code [16] but differ in the way the exact shape of the grains is described. Section 3 then introduces new methods enhancing AOR studies, namely a systematic definition of the AOR value after detection of the

external slope and versatile measurement methods of the packing compacity (void ratio) of the heap since the latter is a fundamental property of granular matter. It also provides a discussion on computational aspects of the two DEM approaches used to simulate the same JGS experiments. Section 4 finally provides new insights on the role of some physical parameters on the AOR value, after conducting a large number of DEM simulations interpreted in a statistics fashion for the sake of robust conclusions.

2 Reference benchmark experiments and DEM formulations

2.1 Reference benchmark experiments

Measurements of AOR data have been recently proposed by the JGS as part of a round robin test organised within the activities of Technical Committee 105 (TC105: Geo-Mechanics from Micro to Macro) of the International Society for Soil Mechanics and Geotechnical Engineering (ISSMGE) [4] and will serve here as reference. In a first step, data only included an experimental characterization of the granular material at hand, together with properties of the two experimental setups used for AOR measurement, before that blind DEM predictions of the AOR values

could be proposed by international participants to the round robin and compared with experimental values [15].

An artificial granular material was considered with non-spherical particles made of 3D-printing resin. Particles constituting the mono-dispersed material resemble a tetrahedral arrangement of four spheres clumped together (see Figure 1). Individual spheres have a radius of $r_s = 0.3101\text{ cm}$, while each global particle is inscribed in a radius $r_{clump} = 0.5\text{ cm}$.

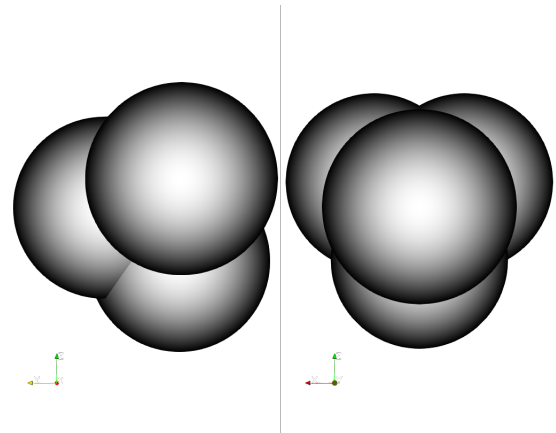


Fig. 1: Physical particle made of 4 clumped spheres.

The considered AOR setups consist of two devices in the form of either a cylindrical (see Figure 2) or cuboidal (see Figure 3) container with acrylic walls, aiming to compare how the AOR varies for heaps of different geometries. For the cylindrical case forming an axisymmetric configuration, the container encloses the particles before the surrounding wall is lowered until a small,

final, height of 1 cm. For the second device corresponding to a plane-strain configuration of the repose state, the cuboidal box encloses the particles initially, until one of the side walls is removed upwards, leaving eventually only a fixed 0.5 cm ridge to retain the lowest particles on that side. The reference number of particles, walls' velocity and boxes' dimensions are given in Table 1 for both configurations, as per the specifications of the round robin test. These parameters were also set to different values for some series of simulations in this study, see Section 4.5 for what concerns the number of particles and boxes' dimensions or Appendix C for the walls' velocity.

2.2 DEM shape description with clump and potential particles approaches

2.2.1 Clumps of spheres

In line with the physical particles at hand (see Figure 1), a first DEM approach adopts the traditional multi-sphere technique to simulate non-spherical particles. A rigid agglomeration of four spheres is created to reflect the particle morphology as a so-called clump, e.g. as shown in [17]. This technique leads to an increased total number of discrete elements in a simulation, compared to the number of physical particles, however it benefits from the low computational cost of collision detection among spheres. To define the inertial

properties of a clump, many DEM codes still simply add the masses of the clump members and directly combine their inertia matrices, which leads to an overestimation in the case of clumps with overlapping members, like the one adopted to simulate the present 3D-printed particle. To mitigate this issue, methods to adjust the density of each sphere-member have been proposed in the literature, such as the one of Ferrellec and McDowell [18] to correct mass and inertia at the cost of some pre-processing efforts. YADE, along with PFC, provide an alternative solution, where a three-dimensional grid of voxels is generated in the bounding box of the particle, and it is evaluated for each voxel whether it belongs to at least one sphere-member of the clump. For the particles at hand in this study, a grid size of $1000 \times 1000 \times 1000$ voxels is used to estimate the volume (and thus the mass) and inertia tensor, with negligible discretisation error induced by the grid resolution, since finer grids led to the same inertial properties.

2.2.2 Potential particles

While the above clump approach is a straightforward DEM strategy for describing the physical particles at hand (Figure 1), a comparison is carried out with a second approach using the so-called "potential particles" introduced by Houlsby [19], and extended to three-dimensions by Boon et al. [20]. The potential particles are generalised convex

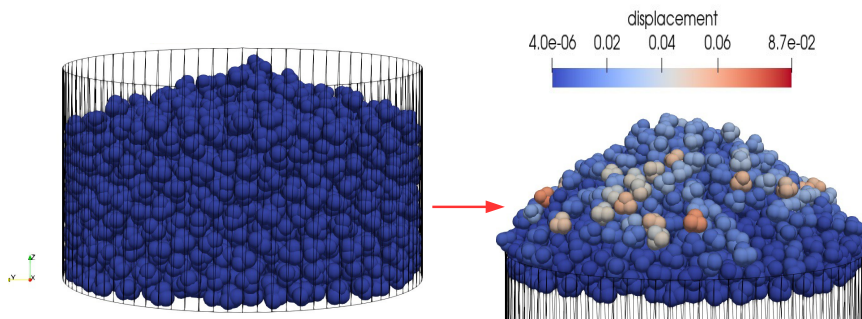


Fig. 2: Initial (left) and final (right) states of the heap in the axisymmetric configuration.

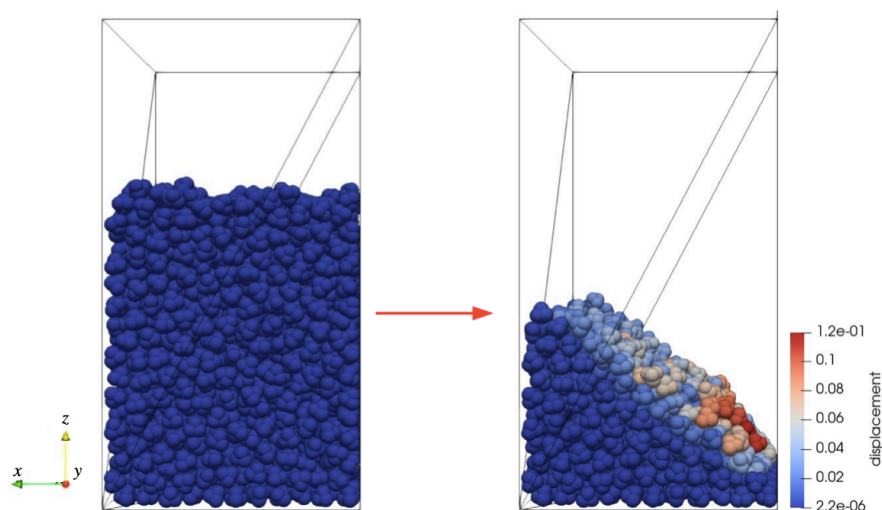


Fig. 3: Initial (left) and final (right) state of the heap in the plane strain configuration.

166 non-spherical particles, assembled as a combina-
 167 tion of 2nd degree polynomial functions and a
 168 fraction of a sphere, while their edges are rounded
 169 with a user-defined radius. In line with their inher-
 170 ent restriction to convexity, rather common in
 171 DEM with complex shapes, e.g. as in [8], the
 172 additional consideration of using potential parti-
 173 cles will illustrate the mechanical implications of

neglecting the concavity of the physical particles
 to the AOR.

For the exact definition of a potential particle,
 as detailed in Boon et al. [20], a set of N planes
 are assembled such that their normal vectors point
 outwards, with their interior forming a convex
 polytope. These planes are summed quadratically
 and expanded by a distance r , which is also related
 to the radius of the curvature at the corners.

Table 1: Default configuration of AOR simulations

Configuration	Initial number of particles	Side wall velocity	Container height	Container width
Axisymmetric	$N_{part} = 2,468$	$V_{cyl} = 6.67 \cdot 10^{-4} \text{ m/s}$	$H_{cyl} = 9 \cdot 10^{-2} \text{ m}$	$R_{cyl} = 8 \cdot 10^{-2} \text{ m}$
Plane strain	$N_{part} = 2,150$	$V_{par} = 4.3 \cdot 10^{-2} \text{ m/s}$	$H_{par} = 1.9 \cdot 10^{-1} \text{ m}$	$L_{par} = 1 \cdot 10^{-1} \text{ m}$

183 Furthermore, a 'shadow' spherical term is added,
 184 where R is its radius and $0 < k \leq 1$ denotes the
 185 fraction of sphericity of the particle. A value of
 186 $k \approx 0$ corresponds to a nearly sharp polyhedron,
 187 while $k = 1$ corresponds to a perfectly spherical
 188 particle.

189 A potential particle is eventually defined by a
 190 potential function f as in Equation 1:

$$f(x, y, z) = (1 - k) \left(\sum_{i=1}^N \frac{\langle a_i x + b_i y + c_i z - d_i \rangle^2}{r^2} - 1 \right) + k \left(\frac{x^2 + y^2 + z^2}{R^2} - 1 \right) \quad (1)$$

191 where (a_i, b_i, c_i) is the normal vector of the i^{th}
 192 plane in local particle coordinates, d_i is the dis-
 193 tance of the plane to the local origin and $\langle \rangle$ are
 194 Macaulay brackets, i.e., $\langle x \rangle = x$ for $x > 0$; $\langle x \rangle = 0$
 195 for $x \leq 0$.

196 This potential function takes zero values ($f =$
 197 0) on the particle surface, negative values ($f < 0$)
 198 inside the particle and positive values ($f > 0$) out-
 199 side. In this sense, some similarity can be found
 200 with the Level-Set Discrete Element Method (LS-
 201 DEM) [21, 22, 23] where the potential is the actual
 202 distance function, unlike here. The contact point
 203 between two potential particles is found as the

optimal point of a Second Order Conic optimi-
 sation Problem (SOCP) describing the contact
 detection problem, representing a point nearest
 to both the particles, based on their potential
 functions.

Here, the mathematical formulation of the
 potential particles enables one to approximate the
 given particle shape by a rounded tetrahedron. To
 decide which planes to use in order to assemble
 the potential particle of the 3D-printed material,
 two criteria were considered, a physical and a
 practical one, with the latter aiming to achieve
 post-processing convenience: (1) First, the poten-
 tial particle should capture the morphology of the
 physical particle as faithfully as possible in terms
 of size, surface curvature, mass and inertia of the
 given physical particle, or other shape descriptors
 such as the sphericity; (2) To achieve comparable
 results with the clump models, for the evaluation
 of the AOR, it is convenient for each potential par-
 ticle to be monitored via four points being located
 at the same positions than the centers of the four
 spheres making the tetrahedron. Thus, it is sought
 that the potential particle has a straightforward
 analogy to this format. To satisfy these criteria,

Table 2: Coefficients defining the planes making the faces of the tetrahedral potential particle as described in Equation 1.

Plane coefficient	Plane 1	Plane 2	Plane 3	Plane 4
a	0	$\sqrt{2/3}$	0	$-\sqrt{2/3}$
b	0	$\sqrt{2/3}$	$2\sqrt{2/3}$	$\sqrt{2/3}$
c	-1	1/3	1/3	1/3
d (cm)	0.063299	0.063299	0.063299	0.063299

the planes used to assemble the potential particle were chosen as the faces of the tetrahedron connecting the centers of the spheres making the physical particle (see Table 2). This approach can be generalised to approximate any convex shape, given a tessellation of its surface, or a multi-sphere representation of a particle made of spheres with equal radii.

To match the local surface curvature of the physical particle, a radius $r = r_s$ was chosen in Equation 1 to control the roundness of the edges and corners of the potential particle consistently with the r_s radius of each individual sphere in the physical particle. The radius of the shadow particle was assigned to $R = \sqrt{2}r_s$, to capture the curvature of faces of the given particle shape. The remaining parameter needed to be calibrated in order to match the given particle shape was the parameter k , which controls the curvature of the faces. A value of $k = 0.65$ led to a good match with the target geometry, i.e. it achieves an adequate representation of both the overall form of the real particle and features such as its main

dimensions, while also approximating its curvature. The parameters r , R and k were chosen via a trial-and-error procedure. Figure 4 demonstrates visually the geometrical faithfulness of the generated potential particle to the shape of the real, physical particle.

In addition to modelling the rounded, tetrahedral-like particles, the potential particles also serve to simulate cuboidal elements of various sizes, making the moving and still parts of the plane-strain and axisymmetric devices, enabling one to build YADE models using a single, unified approach and contact detection algorithm.

2.2.3 Particle shape characterisation

As demonstrated in Figure 4, the selected potential particle can approximate the morphology of the physical particle faithfully, as it qualitatively represents the main dimensions of the particle, determining particle form, along with the curvatures of its edges/corners, relating to particle roundness. However, the potential particles modelling approach cannot represent the concavity of the physical particle. A quantitative characterisation of particle form was also performed using SHAPE [24], an open-source shape analysis software for three-dimensional particles, in order to quantify in Table 3 the similarity between the physical particle and its two numerical replicates. To this end, the surface mesh of the physical particle was first tessellated from its corresponding DEM

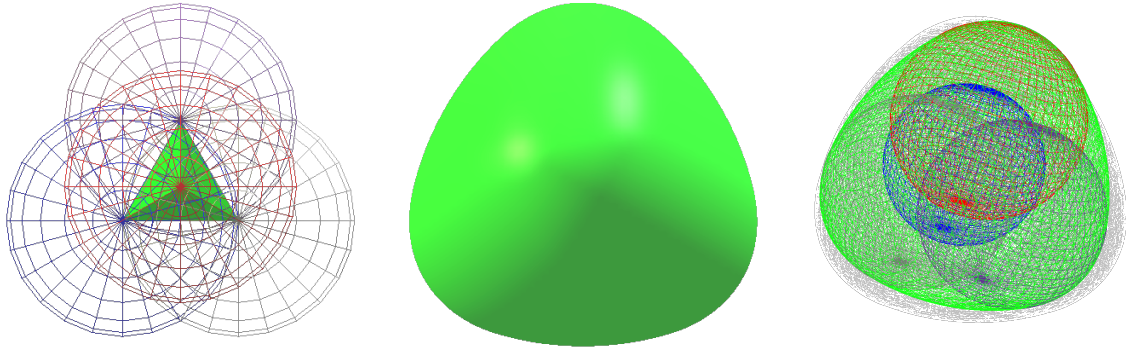


Fig. 4: Clumped tetrahedral particle (left); fitted potential particle (middle); overlap of the two (right).

282 clump, using the surface extraction module of
 283 CLUMP [17], an open-source code for the generation
 284 and processing of multi-sphere particles. Particle
 285 shape was characterised in terms of volume, sur-
 286 face area, principal inertia values, convexity and
 287 true sphericity. Convexity is calculated in [0;1] as
 288 the ratio of the volume of each particle divided by
 289 the volume of its convex hull, while true sphericity,
 290 also ranging in [0;1], is the ratio of the surface area
 291 of a sphere with equal volume to the surface area
 292 of the particle [25]. It becomes evident from Table
 293 3 that both the physical and the potential particle
 294 take high values of convexity and true sphericity
 295 (>0.90). It may furthermore be noted that both
 296 the multi-sphere and the potential particle share
 297 the same minimal bounding box and thus main
 298 particle dimensions, resulting to the same flatness
 299 and elongation values considering indices that rely
 300 on these main particle dimensions. Therefore, flat-
 301 ness and elongation were not monitored in this
 302 study, as convexity and true sphericity were the

two differentiating factors between the two stud- 303
 304 ied particle representations, from a morphological
 305 standpoint. Table 3 also offers a comparison with
 306 a so-called "non-uniform density" clump approach
 307 that would count multiple times the overlapping
 308 parts of the sphere-members in the calculation of
 309 volume and inertia, which would correspond to
 310 density showing a spatial increase at areas where
 311 spheres overlap.

As expected, the considered potential parti- 312
 313 cle has larger values of volume and geometric
 314 inertia. The effect of the resulting increased parti-
 315 cle mass is investigated in Section 4.1 by scaling
 316 down their density so the potential particle has
 317 the same mass as the real particle, i.e. $\rho_{rescaled} =$
 318 $\rho \times 3.3304 \times 10^{-7} / (3.9248 \times 10^{-7}) \approx 943 \text{ kg/m}^3$.

Bringing the error on mass down to zero 319
 320 through this scaling, the error in inertia values for
 321 potential particles drops from 27.17 % down to
 322 7.96 %. It is interesting to note that using over-
 323 lapping spheres with no correction for uniform

Table 3: Shape parameters of the physical particle in comparison with various DEM approaches

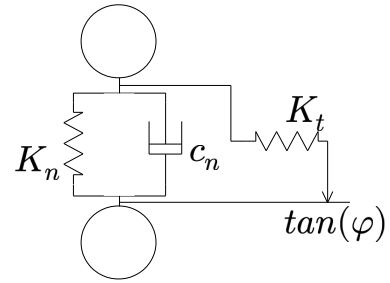
Shape characteristics	(1) Physical particle or present clump approach	(2) Potential Particle	$\frac{(2)-(1)}{(1)}$	(3) Clump approach with non-uniform density	$\frac{(3)-(1)}{(1)}$
Volume (m ³)	3.3304×10^{-7}	3.9248×10^{-7}	17.85%	4.9965×10^{-7}	50.03%
Surface area (m ²)	2.491×10^{-4}	2.632×10^{-4}	5.66%	2.491×10^{-4}	0
Inertia tensor/ ρ (m ⁵)	$\begin{bmatrix} 2.584 & 0 & 0 \\ 0 & 2.584 & 0 \\ 0 & 0 & 2.584 \end{bmatrix} \times 10^{-12}$	$\begin{bmatrix} 3.286 & 0 & 0 \\ 0 & 3.286 & 0 \\ 0 & 0 & 3.286 \end{bmatrix} \times 10^{-12}$	27.17%	$\begin{bmatrix} 3.123 & 0 & 0 \\ 0 & 3.123 & 0 \\ 0 & 0 & 3.123 \end{bmatrix} \times 10^{-12}$	20.86%
Convexity	0.954	1	4.82%	0.954	0
True sphericity	0.9328	0.9849	5.59%	0.9328	0

density i.e. inner overlaps would lead to an error of 50.03 % for the volume and 20.86 % for the eigenvalues of the principal inertia tensor.

2.3 DEM contact formulation

At each contact, kinematics is defined with the normal and tangential relative displacements of the particles, u_n and \underline{u}_t respectively. For the clump model, contacts are detected between spheres belonging to different clumps and u_n is computed as the norm of the branch vector to the spheres' radii, while \underline{u}_t is computed incrementally, see e.g. [23]. For the potential particle model, u_n is computed using a bracketed line-search algorithm as detailed in Boon et al. [20], deployed along the contact normal direction and starting from the contact point, to detect two points on the surface of each particle, forming a branch vector, the norm of which is considered as the sought approaching distance. The shear increment of \underline{u}_t is calculated in a similar manner as for spheres, i.e. via time integration of the shear component of the relative velocity during contact.

The same contact model applies to these kinematic quantities for both the clump and the potential particle approaches, accounting for linear visco-elasticity and friction (Figure 5). In the

**Fig. 5:** Contact model with visco-elasticity and friction.

normal direction, a spring with a normal stiffness K_n is associated in parallel with a viscous damper of coefficient c_n , as formulated in Equation 2. In the tangential direction, a spring with a tangential stiffness K_t is associated in series with a frictional slider (contact friction angle φ), see Equation 3.

$$F_n = \max(K_n u_n + c_n \dot{u}_n, 0) \quad (2)$$

$$|\underline{F}_t| = \min(K_t |\underline{u}_t|, F_n \tan(\varphi)) \quad (3)$$

One should note that different YADE classes implement the above Eqs. 2-3 for clumps and potential particles with different methods of expressing the viscous damping coefficient c_n . In all cases, a desired normal restitution coefficient e_n serves a starting point before some differences appear in the YADE workflow, as detailed in Appendix A. Nevertheless, Figure 6 illustrates the common dissipative behavior of both models with the same $F_n(u_n)$ curves in the case of two colliding spheres (obtained after using $k = 1$ in Equation 1 for the PP approach) with an initial relative normal velocity V , demonstrating the consistency of the two implementations of visco-elasticity.

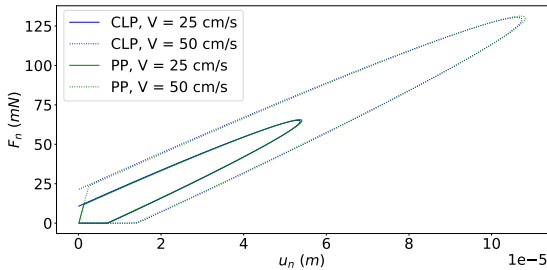
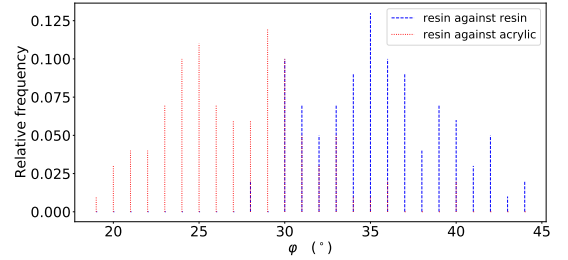


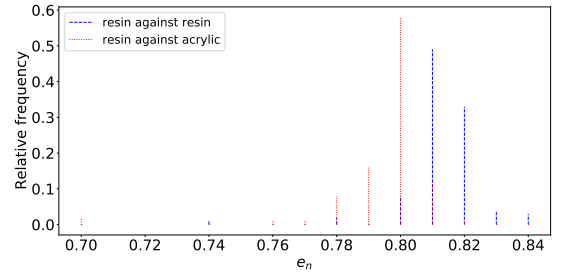
Fig. 6: Contact behaviour for different impact velocities in the two DEM approaches.

In the framework of the round robin test, the JGS measured the contact friction angle φ and the normal restitution coefficient e_n for resin against acrylic contacts and for resin against resin contacts, as well as the normal stiffness K_n for resin spheres. Experimental measurements exhibited a variability and are thus given as distributions (see Figure 7). Unless specified otherwise, the DEM

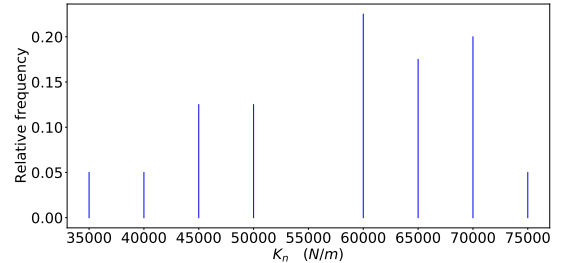
clump simulations are defined accordingly, assigning to all contacts random values of φ and c_n which respect the same distributions.



(a) Contact friction angles for particle/particle ($\varphi_{p/p}$) or particle/wall ($\varphi_{p/w}$) contacts



(b) Restitution coefficient



(c) Normal stiffness

Fig. 7: Distributions of contact properties as experimentally measured by the JGS (adapted from [4])

2.4 DEM simulation workflow

Building DEM samples starts with generating randomly in space particles inside the cuboidal or cylindrical containers mentioned in the above

385 Section 2.1, so as to form a extremely loose assem-
386 bly of non-overlapping particles. The assembly
387 is then deposited under its own weight until it
388 becomes stable, and is saved to be subsequently
389 used under different conditions. Different samples
390 can be obtained starting from different initial par-
391 ticle arrangements. For this first step that has no
392 experimental counterpart, an extra, non-physical,
393 damping source is added in the local, non-viscous,
394 form (Cundall's damping) to speed up the genera-
395 tion. For the rest of the simulations, contact-scale
396 viscous damper and friction solely ensure the sta-
397 bilisation of the simulations and no other source
398 of damping is used.

399 The actual AOR simulation starts from this
400 initial state by displacing the moving parts of the
401 container in a manner equivalent to the exper-
402 iments. Particles leaving the container from its
403 periphery are counted as so-called lost particles
404 and erased for computational efficiency. The sim-
405 ulation continues until the sample finds a new
406 equilibrium in the form of a static heap. It is then
407 possible to measure the angle between its exte-
408 rior surface and the horizontal plane following the
409 procedures discussed below.

410 The default set of parameters for this numeri-
411 cal setup is the experimental one previously given
412 in Table 1.

3 Methodological discussion 413

3.1 Computational aspects of each 414 modelling approach 415

416 In order to provide an overlook of the compu-
417 tational implications of the two considered DEM
418 strategies for shape description, Figure 8 gives
419 a comparison of the computation performances
420 observed during 30 different simulations with both
421 modelling approaches, in terms of computation
422 speed S and Cundall's number $N_C = N_{part}S$.
423 These simulations, presented in more details in
424 Section 4.3, were run sequentially using a Intel(R)
425 Xeon(R) Platinum 8270 CPU @ 2.70GHz with
426 1.5 TB of RAM available. Note that during all
427 series of simulations in this paper the CPU cache
428 wasn't controlled. Its capacity of 35.75 MB may
429 thus not have been used as much over all simula-
430 tions, making the time measurements somewhat
431 biased.

432 Note that heaps may reach equilibrium at dif-
433 ferent simulated times; as a consequence, less and
434 less values were available to compute the mean
435 and standard deviation, until eventually there was
436 only one. The results show that for these simula-
437 tions, the clump model is approximately 100 times
438 faster than the potential particle model. Consider-
439 ing that the present physical particles are simple
440 to describe in a clump approach, using only 4

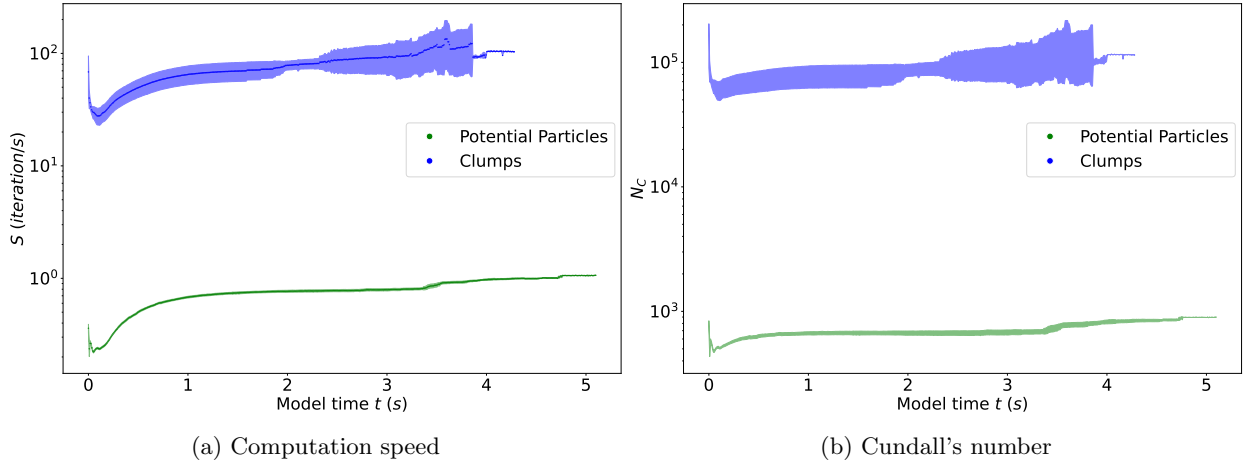


Fig. 8: Computation speed statistics during 30 simulations with each DEM approach (either potential particles or clump, see Section 4.3 for details). Dots represent the mean speed value with the surrounding filled area corresponding to its standard deviation.

441 spherical members, the increased effort in compu-
 442 tational time when using potential particles is in a
 443 classical order of magnitude for DEM approaches
 444 for non-spherical particles [23].

445 3.2 A systematic determination of 446 the angle of repose

447 This section proposes two rigorous methods to
 448 measure the AOR, first, by defining an outer sur-
 449 face of particles and second, by computing an
 450 angle from these particles positions.

451 3.2.1 Outer surface detection

452 In the axisymmetric case (respectively plane strain
 453 case), the 3D space is discretized in several subdo-
 454 mains $\{r; \theta \in [\theta_a, \theta_b]; z \in [z_a, z_b]\}$ (respectively
 455 $\{x \in [x_a, x_b]; y \in [y_a, y_b], z\}$), giving an intersec-
 456 tion with the outer surface at $\max(r)$ (respectively
 457 $\max(z)$) in each subdomain. The extent of each

interval is selected such that only one particle 458
 should be therein detected as belonging to the 459
 outer surface. For such a purpose, length scales L_η 460
 are used for the coordinates θ, z in the axisymmet- 461
 ric case and x, y in the plane strain case. The index 462
 η can represent each of these coordinates. The 463
 number of intervals on each coordinate is then: 464

$$N_\eta = \frac{L_\eta}{d_{clump}} - 1 \quad (4)$$

with $L_\theta = 2\pi R_{cyl}$, $L_z = H_{cyl}$, $L_x = L_{par}$, and 465
 $L_y = H_{par}$. 466

$$\theta_a^i = i \frac{2\pi}{N_\theta}; \quad \theta_b^i = (i+1) \frac{2\pi}{N_\theta} \quad (5)$$

with $i \in \llbracket 0; N_\theta \rrbracket$

$$\eta_a^i = i \frac{L_\eta}{N_\eta}; \quad \eta_b^i = (i+1) \frac{L_\eta}{N_\eta} \quad (6)$$

with $i \in \llbracket 0; N_\eta \rrbracket, \eta \in \{x, y, z\}$

467 Figure 9 shows a typical result after detect-
 468 ing all the particles belonging to the outer surface
 469 in both configurations. Note that gravity has the
 470 opposite orientation of the z-axis.

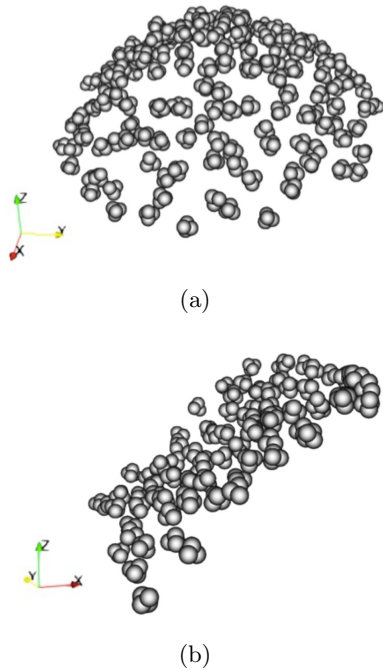


Fig. 9: Outer surface in the axisymmetric (a) and plane strain configurations (b).

in the plane strain case.

Assuming a \tilde{z} -invariance of the heaps, we project the spheres on the (\tilde{x}, \tilde{y}) planes (see Figure 10) and perform a linear regression on the resulting points to determine the AOR α . Letting the linear regression be $\tilde{y}_1 = a_1\tilde{x} + b_1$, one has:

$$\alpha = \arctan(a_1) \quad (7)$$

Consistently with [13, 14], one can notice that the surface isn't exactly flat but slightly curved (especially in the axisymmetric configuration). It can thus be useful to compute a second degree regression as well in order to fit the outer surface in the best possible way. Letting the second degree regression be $\tilde{y}_2 = a_2\tilde{x}^2 + b_2\tilde{x} + c_2$, one can compute a local angle:

$$\alpha(\tilde{x}) = \arctan(2a_2\tilde{x} + b_2) \quad (8)$$

To make the measurement more meaningful, one may naturally restrict the procedure to a smaller zone of the heap: the particles considered in the regressions would only be the ones inside an interval $[\tilde{x}_{min}, \tilde{x}_{max}]$. Indeed, the lower particles may be abruptly blocked by the bottom ridge of the container devices and should be excluded from the measurement. Also, particles with a high \tilde{x} , away from the opened boundary, could be unaffected by the discharge and still form a horizontal

3.2.2 Angle of repose measurement

From this point the method is the same in both heap configurations except for the orientation of the horizontal axis. The coordinates $(\tilde{x}, \tilde{y}, \tilde{z})$ will thus denote respectively $(-r, z, \theta)$ in the axisymmetric case or (x, z, y) in the plane strain case. The width of the container \tilde{x}_{box} for instance stands for R_{cyl} in the axisymmetric case and L_{par}

504 surface, especially in the axisymmetric configura-
 505 tion. Indeed, finite particle-size effects necessarily
 506 exist and affect the transition from one side of the
 507 slope to another.

508 Excluding from the bottom of the heap the
 509 few particles that are stuck by the ridge, and only
 510 those, is obtained choosing: $\tilde{x}_{min} = 0.32d_{clump}$.
 511 An appropriate value for \tilde{x}_{max} is sought by mea-
 512 suring α for several \tilde{x}_{max} . The best \tilde{x}_{max} is the
 513 smallest for which the measurement does not
 514 change. The error on the measurement is also a
 515 criterion to choose the best \tilde{x}_{max} . This method
 516 should be specially relevant in the axisymmetric
 517 case since the outer surface is curved, but it should
 518 work on the plane strain heap as well.

519 3.2.3 Error on the measurement

520 For a given heap, the dispersion of positions data
 521 induces some error on the linear regression and the
 522 measurement of α . As an alternative to the corre-
 523 lation coefficient R^2 , this error can be quantified
 524 from a standard deviation on the slope a_1 of the
 525 fitting line, $\text{StD}(a_1)$. If N is the number of points
 526 and $(\tilde{x}_i, \tilde{y}_i)$ are the coordinates of the i^{th} point,
 527 one has:

$$\text{StD}(a_1) = \sqrt{\frac{1}{N-2} \frac{\sum_{i=1}^N (a_1 \tilde{x}_i + b_1 - \tilde{y}_i)^2}{\sum_{i=1}^N (\tilde{x}_i - \bar{\tilde{x}})^2}} \quad (9)$$

(10)

which, considering Equation 7, gives the standard
 deviation on the angle, $\text{StD}(\alpha)$:

$$\text{StD}(\alpha) = \frac{\text{StD}(a_1)}{1 + a_1^2} \quad (11)$$

528 Figure 10 shows the regressions made on the
 529 projection of the outer surface in both configura-
 530 tions and the resulting angle for $\tilde{x}_{max}/\tilde{x}_{box} = 0.4$,
 531 with $\tilde{x}_{box} \in \{R_{cyl}, L_{par}\}$. Figure 11 shows mea-
 532 surements performed for several \tilde{x}_{max} in both
 533 configurations. The error bars represent the error
 534 computed with Equation 11. One can see that the
 535 AOR increases with \tilde{x}_{max} , except for very high
 536 values of \tilde{x}_{max} where the part of the outer sur-
 537 face considered is very small compared to its size.
 538 This may be caused by the ridge on the bottom
 539 of the open container that maintains some parti-
 540 cles, affecting the geometry of the outer surface.
 541 The error on the measurement is very low but
 542 increases with \tilde{x}_{max} . The measurement is more
 543 stable for low \tilde{x}_{max} , specially in the axisymmet-
 544 ric case. From now on, the measurements will be
 545 performed on most of the outer surface, using
 546 $\tilde{x}_{min} = 0.32d_{clump}$ and $\tilde{x}_{max} = \tilde{x}_{box}$.

547 3.2.4 Error due to repeatability

548 The simulations performed with the clump model
 549 include two sources of randomness. The first one
 550 is the initial configuration of the sample, with ran-
 551 dom positions for the particles in the initial cloud.

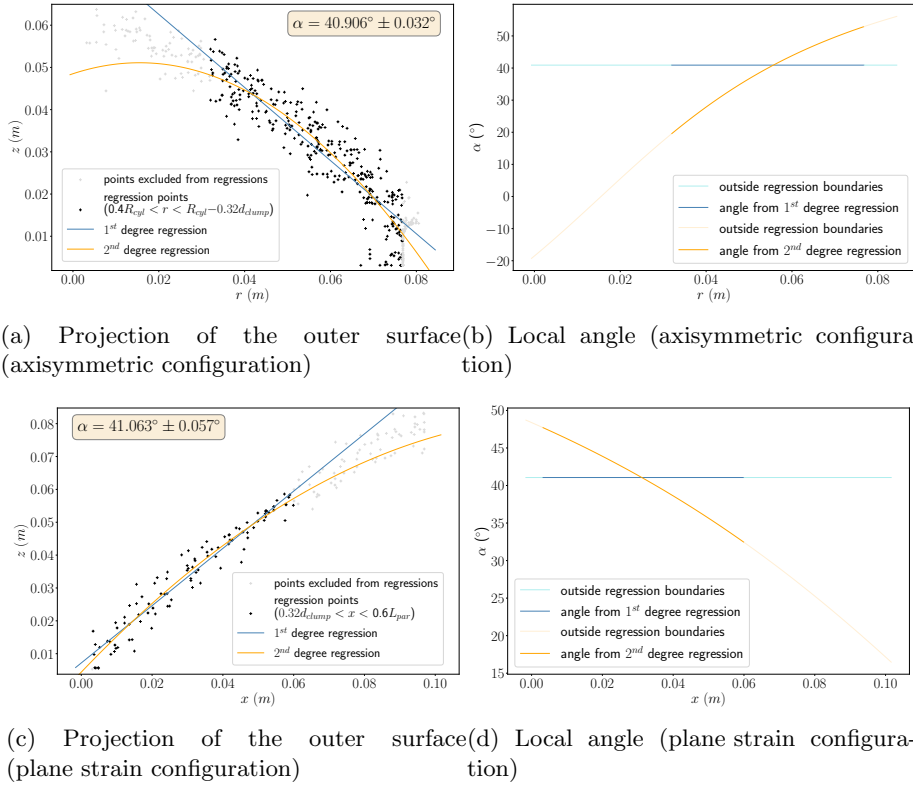


Fig. 10: Outer surface regressions for an intermediate \tilde{x}_{min} and the associated measurement ((a), (c)) in both configurations.

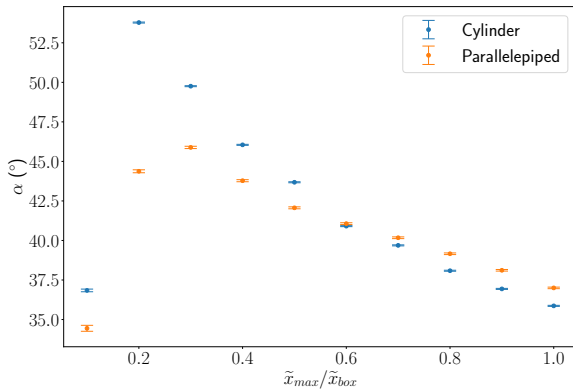


Fig. 11: Average slope as measured for different values of \tilde{x}_{max} .

implies choosing a different value for each contact, all values being randomly chosen according to the given probability distribution. If one was to swap the values of two contacts, the distribution would still be respected, but the conditions of the simulation would be different, introducing randomness.

In order to quantify the repeatability error, a series of simulations was performed with the clump model using 30 different values for the seed parameter, the particles in the initial samples of each simulation thus have different positions and contact properties. This series will be called

The second source lies in the statistical distribution of contact properties (see the above Figure 7). Indeed, the use of distributions for φ and e_n

CLP1 and uses the default parameters of Table 4. Among those parameters, the time step is computed from contact stiffnesses and particle masses following [26]. Note that all samples have approximately the same initial densities. Figure 12 shows the AOR measured using CLP1 heaps and one can see that the variation in the measurement is lower than 3%. Even though such a repeatability error is low, it will be systematically given for all series of simulations in this paper as error bars on the AOR charts.

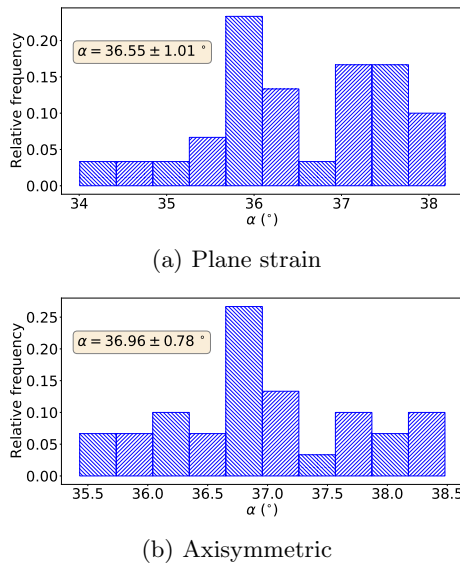


Fig. 12: Distributions of measured angles of repose when investigating repeatability in the CLP1 configurations of Table 4.

3.3 Measuring the void ratio for any geometry of assembly

With respect to the objective of discussing the possible constitutive nature of the AOR determined as per Section 3.2, it is interesting to characterize the state of the heap in terms of density or void ratio e , as a fundamental parameter of granular materials. This density characterization is not straightforward because of the irregular geometry of the heap along its free surface, and possible bias caused by an excess of void near the walls

As such, two methods are proposed below to compute the void ratio inside a granular assembly with a complex geometry, while avoiding the boundary effects: a so-called "tetrahedra method" and a "sub-volume method". Both methods provide local values for e and rely on a Monte Carlo procedure to compute volume proportions, combined with (straightforward, here) tests to determine whether a random point in space is inside a physical particle. The following differences still exist, though:

- the tetrahedra method applies for any geometry of sample with no requirements on the geometry. It is based on a triangulation of the sample.
- the sub-volume method requires to define an homothetic sub-volume inside the sample,

Table 4: Parameters for heap simulations investigating repeatability (CLP1 series, 60 simulations in total).

Configuration	N_{part}	$\frac{K_n}{(N.m^{-1})}$	K_s/K_n	$\frac{\rho}{(kg.m^{-3})}$	Δt (s)	φ	e_0	Number of samples
Plane strain	2,150	58,250	0.37	1,111	7.86×10^{-5}	see	0.622 ± 0.012	30
Axisymmetric	2,468					Figure 7	0.744 ± 0.028	

which can be difficult if the latter adopts a peculiar geometry. However, it is substantially faster than the tetrahedra method.

3.3.1 The tetrahedra method

In order to compute a void ratio on a heap with a random geometry, the tetrahedra method starts by a triangulation of the heap. The Monte Carlo method is then used to determine the proportion of particles inside each tetrahedron resulting from the triangulation, leading to an expression for the void ratio.

3.3.1.1 Triangulating the heap

This first step is done using Delaunay's triangulation on the centers of all particles, although it could be done using another set of relevant points (e.g. the center of all spheres for clump simulations). Also, one should keep in mind that when triangulating using the center of the particles a small part of the sample is ignored: all particles on the outer surfaces are cut by the boundary tetrahedra. This should effectively remove the excess of

void near the walls of any sample. The set of all tetrahedra will be denoted $\{tet\}$.

3.3.1.2 Detecting which particle may be partially inside each tetrahedron

All particles bounding boxes are tested to determine if they overlap a tetrahedron bounding box. If so, the particle is further checked for intersected volume with the Monte Carlo method, forming a set of particles that is denoted $\{p\}^{cut}$. This step is not mandatory but it drastically reduces the computation time.

3.3.1.3 Computing the total volume of particle inside each tetrahedron

In this final step, N_{mc} points $\{\underline{x}_i, i \in [1, N_{mc}] \cap \mathbb{N}\}$ are uniformly drawn inside the tetrahedron, following [27]. Each point is tested to determine if it is located inside any of the particles potentially cut $\{p\}^{cut}$. Denoting V^{tet} the volume of a tetrahedron tet computed using its vertices' coordinates; $\chi^p(\underline{x})$ the Boolean test function equal to

656 1 if the point \underline{x} is inside the particle p , 0 otherwise;
 657 and $H(n)$ the Heaviside function, the Monte-Carlo
 658 method gives the total volume of particle inside
 659 the tetrahedron as follows:

$$V_{part}^{tet} = \frac{\sum_{i=1}^{N_{mc}} H\left(\sum_{\{p\}^{cut}} \chi^p(\underline{x}_i)\right)}{N_{mc}} \times V^{tet} \quad (12)$$

660 A local void ratio can then be computed for
 661 the tetrahedron:

$$e^{tet} = \frac{V^{tet} - V_{part}^{tet}}{V_{part}^{tet}} \quad (13)$$

And globally:

$$V_{part} = \sum_{\{tet\}} V_{part}^{tet} \quad (14)$$

$$V_{tot} = \sum_{\{tet\}} V^{tet} \quad (15)$$

$$e = \frac{V_{tot} - V_{part}}{V_{part}} \quad (16)$$

662 Taking advantage of the independence between
 663 operations in each tetrahedron, the proposed
 664 implementation of this method is parallel with an
 665 almost optimal speed-up: the increase in execution
 666 speed is close to the number of processes running
 667 at the same time.

668

669 3.3.2 The sub-volume method

670 The sub-volume method consists in three steps
 671 detailed below.

3.3.2.1 Defining the sub-volume

672

673

674

This step is illustrated using the two samples' geometries considered in this paper. The sub-volume is chosen as a homothetic transformation of the heap centered in the sample, for both configurations. The sub-volume and the total volume of the sample will be denoted V_{sub} and V , respectively. At the final state, the geometry of the sample is assumed to be a half parallelepiped (respectively a cone) for the plane strain (respectively axisymmetric) configuration. The sub-volume is defined using a parameter C that pilots the homothetic transformation. The coordinates of the sub-volume axis aligned bounding box are denoted $(x_{min}, y_{min}, z_{min})$ and $(x_{max}, y_{max}, z_{max})$ and depend on the coordinates of the sample axis aligned bounding box: $(X_{min}, Y_{min}, Z_{min})$ and $(X_{max}, Y_{max}, Z_{max})$.

675

676

677

678

679

680

681

682

683

684

685

686

687

688

689

690

691

In the case of the plane strain configuration, the homothetic sub-volume can be determined as follows (Figure 13):

692

693

694

$$s_{min} = (1 - C)(S_{max} - S_{min}) + S_{min} \quad (17)$$

$$s_{max} = C(S_{max} - S_{min}) + S_{min} \quad (18)$$

with $\forall (s, S) \in \{(x, X), (y, Y), (z, Z)\}$ and $\forall C \in]0.5, 1]$.

695

696

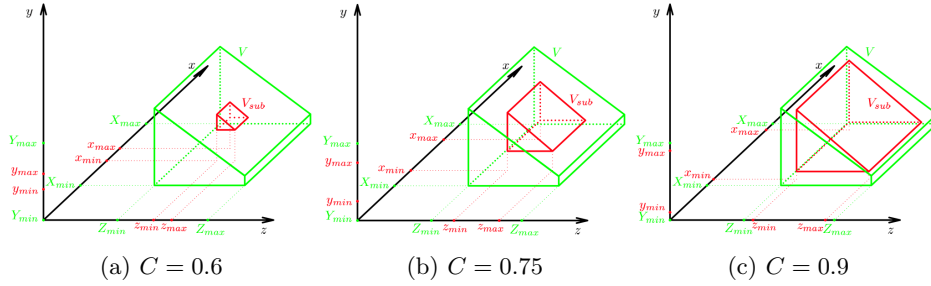


Fig. 13: Illustration of sub-volume for several C values in the plane strain configuration.

697 In the case of the axisymmetric configuration,
 698 one has to compute the x and y coordinates of the
 699 center, x_Ω and y_Ω respectively, and the maximum
 700 radius r_c of the cone (Figure 14). The homothetic
 701 sub-volume is then:

$$z_{min} = (1 - C)(Z_{max} - Z_{min}) + Z_{min} \quad (19)$$

$$z_{max} = C(Z_{max} - Z_{min}) + Z_{min} \quad (20)$$

$$s_\Omega = \frac{S_{min} + S_{max}}{2} \quad (21)$$

$$r_c = (2C - 1) \frac{X_{max} - X_{min} + Y_{max} - Y_{min}}{4} \quad (22)$$

702 with $\forall (s, S) \in \{(x, X), (y, Y)\}$ and $\forall C \in]0.5, 1]$.

703 3.3.2.2 Counting the volume of particles 704 completely inside the sub-volume

705
 706
 707 During this step, the 8 vertices \underline{x}_i^p of a particle
 708 axis aligned bounding box are tested to deter-
 709 mine if they are part of the sub-volume. Using the

$\chi^{sub}(\underline{x})$ function, the number of vertices inside the
 710 sub-volume for a particle p reads:
 711

$$N_{in}^p = \sum_{i=1}^8 \chi^{sub}(\underline{x}_i^p) \quad (23)$$

If $N_{in}^p = 8$, the particle p is completely inside
 712 the sub-volume while if $N_{in}^p = 0$ the particle p is
 713 completely outside the sub-volume.
 714

Denoting V^p the volume of the particle p , the
 715 total volume of particles completely inside the
 716 sub-volume is:
 717

$$V_{part}^{in} = \sum_{\{p \mid N_{in}^p=8\}} V^p \quad (24)$$

718 3.3.2.3 Counting the volume of particles 719 partially inside the sub-volume

720
 721
 722 If $0 < N_{in}^p < 8$, the particle may be cut by
 723 the faces of the sub-volume. The proportion of
 724 the particle volume inside the sub-volume is again
 725 determined using the Monte Carlo method: N_{mc}
 726 points, $\{\underline{x}_i, i \in \llbracket 1; N_{mc} \rrbracket\}$, are uniformly drawn
 727 inside the particle bounding box and tested to

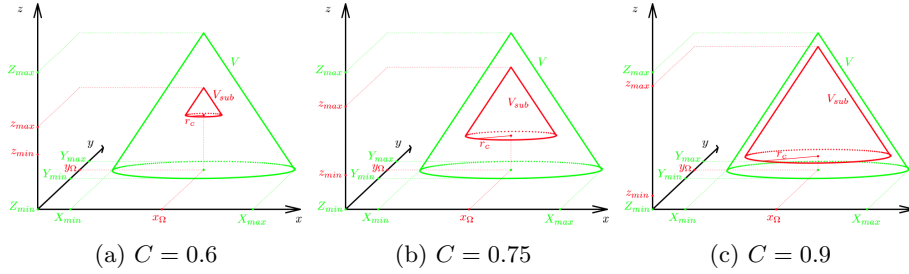


Fig. 14: Illustration of sub-volume for several C values in the axisymmetric case.

728 determine if they are simultaneously inside the
 729 sub-volume (test function $\chi^{sub}(\underline{x}_i)$) and inside the
 730 particle (test function $\chi^p(\underline{x}_i)$). The proportion of a
 731 particle volume being also part of the sub-volume
 732 is then:

$$V_{in}^p = \frac{\sum_{i=1}^{N_{mc}} \chi^{sub}(\underline{x}_i) \chi^p(\underline{x}_i)}{N_{mc}} \times V^p \quad (25)$$

733 The total volume of particles partially inside
 734 the sub-volume is:

$$V_{part}^{cut} = \sum_{\{p \mid 0 < N_{in}^p < 8\}} V_{in}^p \quad (26)$$

735 The total volume of particle inside the sub-
 736 volume then reads:

$$V_{part} = V_{part}^{in} + V_{part}^{cut} \quad (27)$$

737 Finally, the void ratio is determined by:

$$e = \frac{V_{sub} - V_{part}}{V_{part}} \quad (28)$$

For the simplest sub-volume geometries the
 expression of V_{sub} is trivial. In more complex sit-
 uations it can be determined using once again
 the Monte Carlo method inside the sub-volume
 bounding box:

$$V_{sub}^{bb} = (x_{max} - x_{min})(y_{max} - y_{min})(z_{max} - z_{min}) \quad (29)$$

$$V_{sub} = \frac{\sum_{i=1}^{N_{mc}} \chi^{sub}(\underline{x}_i)}{N_{mc}} \times V_{sub}^{bb} \quad (30)$$

Both methods can be optimized when used
 with simple shapes (e.g. spheres): one could detect
 more precisely which particle may be cut. Also,
 one may be able to draw uniformly points directly
 inside the particle instead of the bounding box,
 making it possible to set aside the function χ^p and
 giving a more accurate Monte Carlo method.

3.3.3 Examples of void ratio

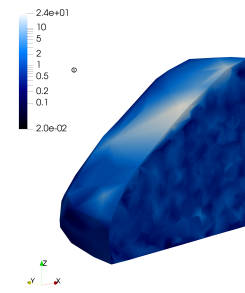
measurements

3.3.3.1 Local void ratio

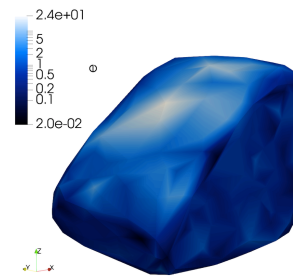
The tetrahedra method makes it possible to establish directly a local representation of the void ratio, as illustrated in Figure 15 for one plane strain final heap. One can notice that the geometry of the final heap is accurately captured by the triangulation, giving a rounded half parallelepipedic boundary surface. The density range is quite wide: some tetrahedra located on the outer surface, where the particles moved, contain approximately 1000 times more voids than other tetrahedra located where the particles almost didn't move. Note that this figure represents the void ratio directly interpolated from the centroids of each tetrahedron and thus should be interpreted carefully.

3.3.3.2 Parallel implementation of the tetrahedra method

The independence of the processing of each tetrahedron makes it possible to parallelize this method. A series of measurements was performed on 30 clump samples at their initial states (showing different individual locations of particles)



(a) Sliced view



(b) Complete view

Fig. 15: Local void ratio in a plane strain final heap as measured with the tetrahedra method.

using different numbers of CPU cores, $N_{cores} \geq 1$, on the same machine previously used in Section 3.1. The speed-up S and its standard deviation ΔS was computed from the computation times $T_{N_{cores}} \pm \Delta T_{N_{cores}}$ as follows:

$$S = \frac{T_1}{T_{N_{cores}}} \quad (31)$$

$$\Delta S = S \left(\frac{\Delta T_1}{T_1} + \frac{\Delta T_{N_{cores}}}{T_{N_{cores}}} \right) \quad (32)$$

Since the CPU cache was not precisely controlled, the total CPU load had an influence on the computation speed, which might lead to a speed-up seemingly above perfection in the eventuality of

the CPU cache being full during the measurement on 1 core and not for more cores.

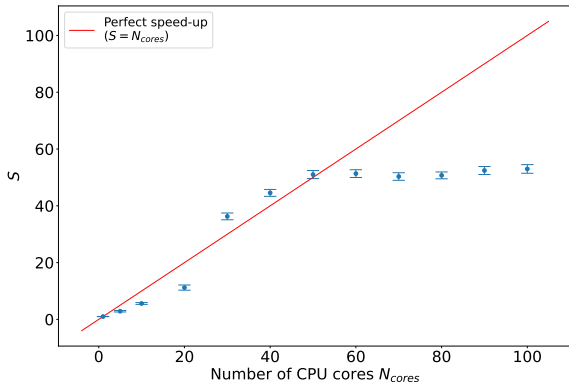


Fig. 16: Parallelization speed-up for the tetrahedra method.

Figure 16 shows the speed-up for $N_{cores} \in \{1, 5, 10, 20, 30, 40, 50, 60, 70, 80, 90, 100\}$. The speed-up stops to improve starting from $N_{cores} = 50$, which is probably due to an over usage of the CPU. A better control of the CPU could give more accurate speed-up measurements. Nevertheless, for $N_{cores} < 50$ the parallelization is optimum: $S \approx N_{cores}$.

3.3.3.3 Sub-volume and tetrahedra methods comparison

Void ratio measurements were performed for the clump model on all 30 initial samples of CLP1 plane-strain series of simulations, discussed in more details in Section 4.3. Because of the

simple parallelepipedic geometry of these granular assemblies, a reference void ratio can be easily computed using the sample bounding box:

$$V_{tot} = (X_{max} - X_{min})(Y_{max} - Y_{min})(Z_{max} - Z_{min}) \quad (33)$$

$$V_{part} = \sum_{\{p\}} V^p, \text{ with } \{p\} \text{ the set of all particles} \quad (34)$$

$$e^{REF} = \frac{V_{tot} - V_{part}}{V_{part}} \quad (35)$$

Figure 17 (a) illustrates the comparison between the mean values and standard deviation over the 30 samples of e^{REF} together with e^{TET} for the tetrahedra method and e^{SUB} for the sub-volume method. The latter has been computed for 3 values of N_{mc} and 40 values of C .

For the lowest values of C , the measured e^{SUB} void ratio varies a lot among the 30 simulations and in function of N_{mc} . Between $C \approx 0.7$ and $C \approx 0.9$, e^{SUB} is constant and its standard deviation gets lower, being furthermore little dependent on N_{mc} . For $C > 0.9$, its mean value and standard deviation finally start to increase as expected due to the rigid boundaries constraining the granular assembly and favoring voids to form near the outer surfaces. Finally, for $C = 1$, the sub-volume method gives by definition the exact same values for void ratio than when using the global bounding box: $e^{SUB} = e^{REF}$.

828 The tetrahedra method gives a e^{TET} measure-
 829 ment being close to e^{SUB} when $0.7 < C < 0.9$,
 830 which suggests that it successfully excludes the
 831 excess of void from the computation.

832 As for the computational costs, Figure 17 (b)
 833 shows the corresponding execution times, t^{SUB} ,
 834 t^{TET} and t^{REF} , while e^{TET} was computed using
 835 parallelization on 3 cores. One observes that, in
 836 spite of parallelization, the tetrahedra method
 837 is here significantly slower than the sub-volume
 838 method. Regarding the sub-volume method, using
 839 $N_{mc} = 1000$ instead of $N_{mc} = 100$ slows down
 840 considerably the computation for no gain in accu-
 841 racy, especially for high values of C .

842 In view of these results, subsequent measure-
 843 ments of void ratio will be obtained using the
 844 sub-volume method with $N_{mc} = 100$ and $C = 0.8$.

845 4 Physical discussion

846 This section analyses the dependence of AOR on
 847 several parameters: the particle shape, the ini-
 848 tial void ratio and the sample size. Experimental
 849 results obtained in [4] are also provided.

850 4.1 Parametric study

851 4.1.1 (Non-)Sensitivity to the 852 tangential stiffness

853 A first series of simulations investigates the role of
 854 tangential stiffness when using the potential par-
 855 ticles model and two different values of K_s : 240
 856 N/m and 444 N/m (see sets B and C of Table 5).

857 Results are given in Figure 18 for what con-
 858 cerns the initial and final states of the samples.
 859 Most importantly, the two different values of tan-
 860 gential stiffness are shown to result in virtually
 861 the same AOR distribution. The $K_s = 240 N.m^{-1}$
 862 value will thus be kept in the remainder of the
 863 sequel for it results in a higher critical time step.
 864 One may furthermore note that the initial coor-
 865 dination number is slightly lower with a higher
 866 K_s , which is expected since stiff particles tend to
 867 be further away from each other, even when con-
 868 strained. However, at the final state, the average
 869 coordination number is unaffected by K_s , cer-
 870 tainly because they are not constrained enough for
 871 their relative distance to depend on K_s .

872 4.1.2 (Non-)Sensitivity to the particle 873 mass density

874 While the AOR α refers to a static condition, the
 875 mass density of particles ρ physically affects the
 876 prior dynamic evolutions of the system. On the
 877 other hand, from a computational standpoint, the
 878 density also controls the critical time step of the

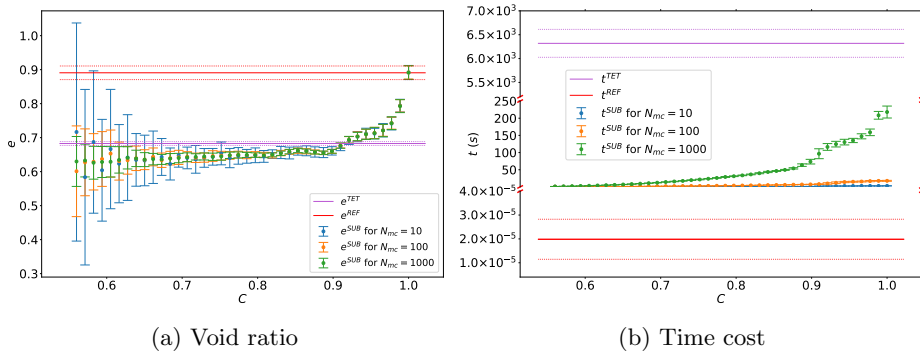


Fig. 17: Void ratio measurements with both methods for 30 parallelepipedic initial samples differing in individual locations of particles. On figure (b), the y axis is broken at two places: first between 40 ns and 50 ms , and second between 250 s and 5200 s . The three parts of the y axis do not have the same scale.

Table 5: Used parameters for the parametric study with potential particles - series PP1.

Set id	Configuration	K_n ($N.m^{-1}$)	K_s/K_n	ρ ($kg.m^{-3}$)	Δt (s)	$\varphi_{p/p}$ ($^\circ$)	$\varphi_{p/w}$ ($^\circ$)	β_n	Number of samples
A	Plane strain	1,200	0.2	1111	8.52×10^{-5}	35.5	27.2	0.071	30
B			0.2	943	7.86×10^{-5}				
C			0.37	943	7.86×10^{-5}				

879 present explicit DEM scheme and the total time
 880 cost. Other series of simulations with different ρ
 881 are thus proposed to check whether a variation
 882 from the experimental reference $\rho = 1,111 \text{ kg/m}^3$
 883 would affect the AOR results.

884 Using potential particles, two values for the
 885 particle density are considered in the framework
 886 of the PP1 series (sets A and B of Table 5):
 887 the experimental one, $\rho = 1,111 \text{ kg/m}^3$, and
 888 $\rho = 943 \text{ kg/m}^3$ that would confer the potential
 889 particle the same mass as the physical parti-
 890 cle in spite of the volume differences discussed
 891 in the above Section 2.2.3. Using clumps in a
 892 CLP2 series, four to seven different values for
 893 $\rho \in [100 \text{ kg/m}^3; 10,000 \text{ kg/m}^3]$ are considered,
 894 with 10 different initial samples in each case.

895 Corresponding parameters are all given in Table
 896 6.

897 Figure 19 shows the resulting angles of repose
 898 in the CLP2 and PP1 series, together with time
 899 costs of CLP1 series measured for a sequential
 900 execution on the same machine presented in previ-
 901 ous Section 3.1. The dots correspond to the mean
 902 measurement over all samples for a given particle
 903 density and the error bars represent the standard
 904 deviation. One can see that all error bars share
 905 a common zone for a given shape description. As
 906 such, it is herein concluded, consistent to [9], that
 907 particle density does not impact the AOR. During
 908 DEM simulations, one can thus adopt, when nec-
 909 essary, an artificial $\rho = 10,000 \text{ kg/m}^3$, multiplying
 910 the critical time step by a factor of $\sqrt{\frac{10000}{1111}} \approx 3$

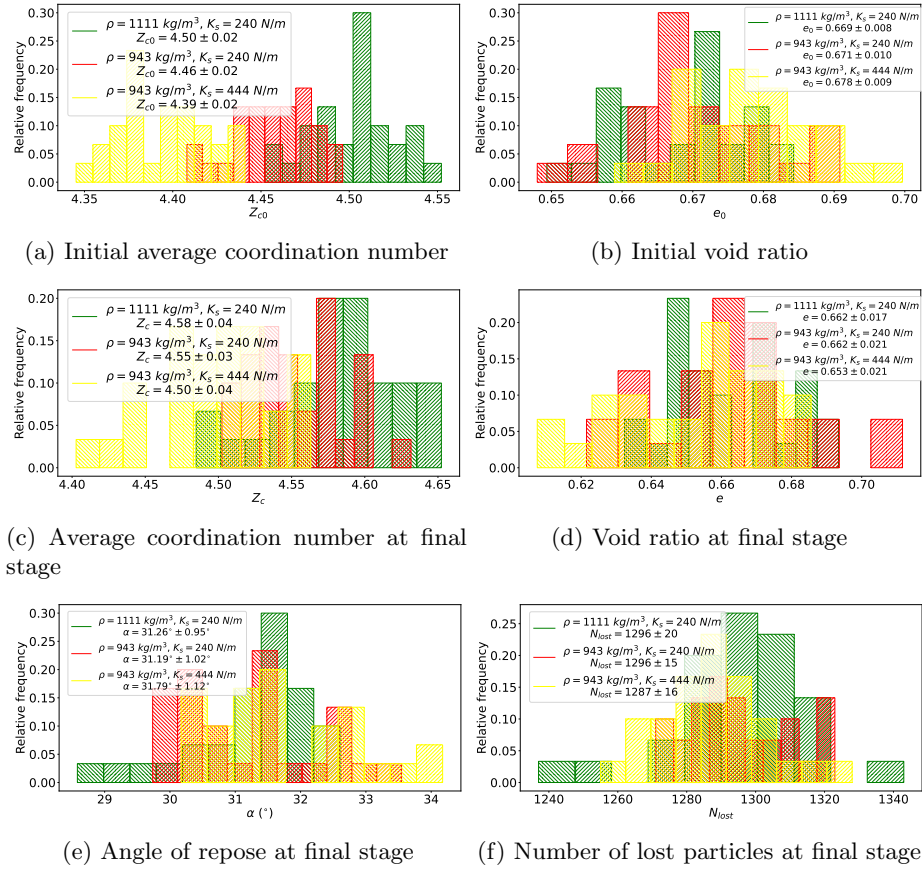


Fig. 18: Macro-scale and micro-scale results of the parametric analysis with potential particles (PP1 series, Table 5).

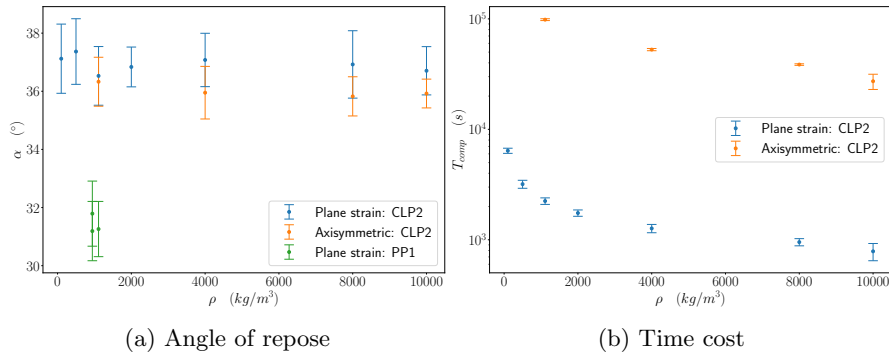


Fig. 19: Particle density influence on the angle of repose and on the time cost - CLP2 and PP1 series

911 and reducing as much as possible the total time cost of the
912 simulation (Figure 19b) until the heap stabilizes.

913 In the Figure 19b, one can finally note a longer

914 computation time for the axisymmetric configuration

915 because of a lower velocity of the descending

916 wall in the reference experiments.

Table 6: Parameters of heap simulations investigating ρ influence (CLP2 series, 110 simulations in total).

Configuration	N_{part}	ρ	ϵ_0	Number of samples
Plane-strain	2,150	100 kg/m^3	0.652 ± 0.011	10
		500 kg/m^3	0.633 ± 0.010	
		1,111 kg/m^3	0.623 ± 0.009	
		2,000 kg/m^3	0.618 ± 0.010	
		4,000 kg/m^3	0.607 ± 0.011	
		8,000 kg/m^3	0.603 ± 0.012	
Axisymmetric	2,468	10,000 kg/m^3	0.603 ± 0.010	
		1,111 kg/m^3	0.743 ± 0.022	
		4,000 kg/m^3	0.723 ± 0.015	
		8,000 kg/m^3	0.709 ± 0.019	
		10,000 kg/m^3	0.694 ± 0.010	

4.2 Numerical angle of repose vs experimental one

The numerical simulations are now compared with the experimental results provided at the end of the JGS round-robin and in [4]. In this framework, a simpler method was adopted to compute the AOR, considering only the highest particle instead of the whole external surface as in previous Section 3.2, for sake of simplicity during the experiments. In the axisymmetric configuration, slopes are actually determined in 360 directions being not exactly radial and their average is used to compute the AOR, while in the plane strain configuration the AOR is computed using only one slope direction in the plane.

In this subsection, the exact same method is adopted to interpret our numerical results for a consistent comparison. The set of parameters used for the clump model is the same as for CLP1 (see Table 4), and the set of parameters used for the potential particle model is given in Table 7.

Table 8 compares the obtained experimental and numerical results. In the plane strain configuration, the experimental AOR is approximately 8% higher than the one obtained for the clump model and 16% higher than the one obtained for the potential particle model. In the axisymmetric configuration, the experimental AOR is approximately 4% higher than the one obtained with the clump model and 16% higher than the one obtained for the potential particle model. Also, one should notice that in the plane strain configuration the JGS method measures an AOR higher than the method presented in this paper, and lower in the axisymmetric configuration (see Figure 12). This changes the conclusion on the influence of the configuration: with our measurement method both configurations gives the same AOR (difference of approximately 1% with the clump model), while the JGS method gives a difference of approximately 11%.

Table 7: Material properties used in the potential particles models.

K_n ($N.m^{-1}$)	K_s/K_n	ρ ($kg.m^{-3}$)	Δt (s)	$\varphi_{p/p}$ ($^\circ$)	$\varphi_{p/w}$ ($^\circ$)	β_n
1200	0.773	943	7.86×10^{-5}	35.5	27.2	0.071

Table 8: Angle of repose as per the JGS measurement method.

	Number of samples	Average ($^\circ$)	Standard Deviation ($^\circ$)	Minimum ($^\circ$)	Maximum ($^\circ$)
Plane strain configuration					
Experiments [4]	400	41.4	1.28	38.3	46.3
Clumps	100	38.1	1.14	35.0	41.3
Potential particles	18	34.8	1.61	32.5	38.0
Axisymmetric configuration					
Experiments [4]	50	35.3	0.9	33.3	37.3
Clumps	100	33.9	0.8	32.0	36.1
Potential particles	19	29.7	0.78	28.5	31.2

4.3 Role of particle concavity

The differences in AOR observed in Table 8 between the clump and potential particle (PP) models, with a higher discrepancy for PP towards experiments, certainly arise from the convex simplification of potential particles, with respect to the concavities of the physical particles which allow them to interlock better. In order to gain more insights into the influence of particle concavity, a rigorous comparison between the two numerical models is led in this subsection, adopting the same parameters for both models (except for the time step for computational efficiency) and determining the AOR using the more reliable method presented in Section 3.2. This series

is called PP-CLP, with all parameters being listed in Table 9 and Table 10.

Figure 20 characterizes the initial and final states of these PP-CLP simulations. First and foremost, it is to notice that the AOR is approximately 14% lower with the potential particle model. This difference can be considered as significant and is even greater with respect to experiments even though the physical particles show a fairly high convexity of 0.954. In line with additional possibilities of interlocking for non-convex particles, while convex particles fall more easily from the heap, the number of lost particles is approximately 23% lower with the clump model. One can also note that the final void ratio is approximately the same with both models and

Table 9: Contact parameters of the PP-CLP series focusing on particle concavity

Model	K_n	K_s	e_n	$\varphi_{p/p}$	$\varphi_{p/w}$
Clump Potential particle	1.2 kN.m^{-1}	0.24 kN.m^{-1}	0.8	35.5°	27.2°

Table 10: Other simulation parameters of the PP-CLP series on particle concavity

Model	Configuration	ρ	Δt	Number of samples
Clump Potential particle	Plane strain	1111 kg.m^{-3}	$\approx 78.5 \mu\text{s}$ $\approx 85.2 \mu\text{s}$	30

that the final average number of contact points per particle is approximately 25% lower with the potential particle model since two convex particles can form only one contact point, unlike the concave clump.

It is worth noticing that the experimental measurement method gives a gap between the axisymmetric and plane strain configurations' angle of repose. The curvature of the axisymmetric heap explains the lower measurement obtained with the JGS method.

Looking at initial stages, one observes that the initial void ratio is approximately 5% lower with the clump model. The difference between the void ratio at the initial state and final state is interesting: at the initial state the sample is constrained by four side walls and one bottom wall, while at the final state one of the four sides of the sample is free. This suggests that concave particles are more likely to fill the voids when they are surrounded by walls (parallel to the gravity axis), but when

they are free to move, they do not fill the voids better than convex particles. On the other hand, the difference on the average number of contact points is approximately the same at the initial and final states.

4.4 (Non-)Constitutive nature of the angle of repose

The compatibility of AOR values measured (with the present method, see Figures 12 and 19) in both axisymmetric and plane strain configurations of the reference device could confirm a constitutive nature of the AOR inferred in, e.g., [5, 6, 7], suggesting to compare the latter with shear strength properties of the granular material. Generally speaking in solid-like granular mechanics, these shear strength properties may refer either to a critical state or a state of maximum stress ratio, the two being possibly different depending on initial porosity.

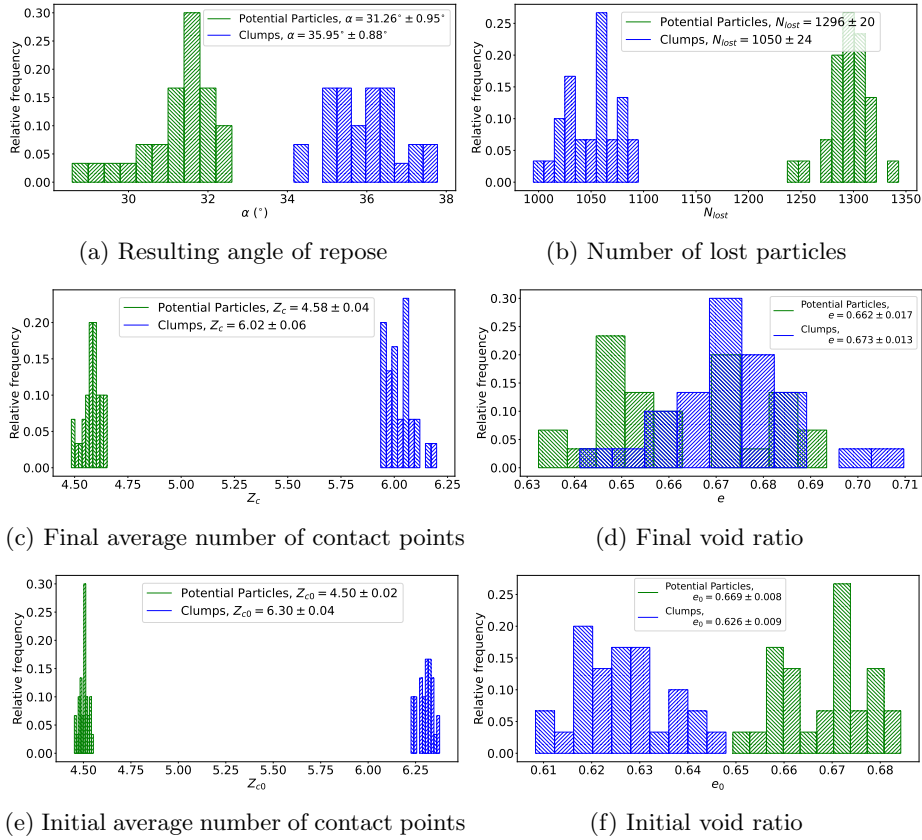
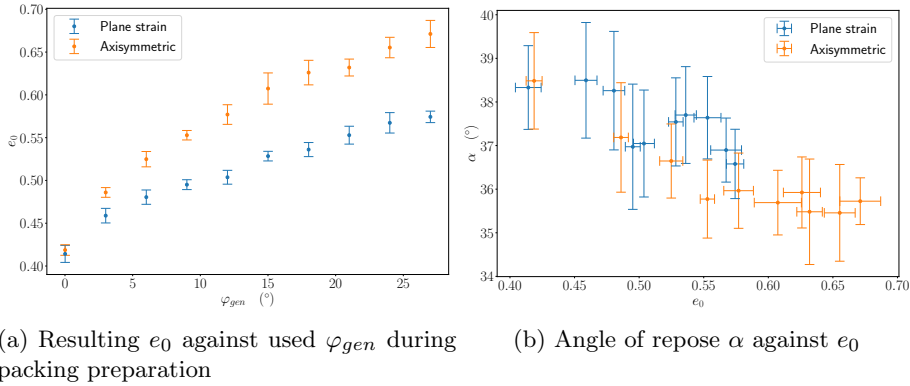


Fig. 20: Characterization of the PP-CLP series on particle concavity in terms of initial and final states

1029 Here, it is first determined whether the AOR
 1030 α evolves with respect to the initial void ratio e_0 ,
 1031 which would contradict the definition of a crit-
 1032 ical state property. This is done by performing
 1033 a “CLP4” series of simulations with the clump
 1034 model using several samples at different initial
 1035 porosities, whose parameters are given in Table 11.
 1036 The initial void ratio e_0 is controlled by momen-
 1037 tarily altering the inter-particle friction angle dur-
 1038 ing the generation of the sample, φ_{gen} , whereby
 1039 lower φ_{gen} -values lead to denser packings, as plot-
 1040 ted in Figure 21 (a) where the error bars represent

1041 the standard deviation of e_0 on all 10 simula-
 1042 tions performed at the same φ_{gen} . Figure 21 (b)
 1043 shows α against e_0 and reveals some decreasing
 1044 tendency of α for $e_0 < 0.55$ in both configurations
 1045 that would be more consistent with an interpreta-
 1046 tion of the AOR in terms of a porosity-dependent
 1047 maximum friction angle. However, the significant
 1048 dispersion of the results prompts the need for
 1049 further investigations in the following.

1050 In addition, it is to note that a critical state
 1051 interpretation of the repose would impose a cor-
 1052 relation between critical state values of porosity
 1053 (or void ratio) and mean pressure p in the form

**Fig. 21:** Influence of the initial void ratio e_0 - CLP4 series

1054 of a critical state line (CSL). Assuming, likewise
 1055 to void ratio e , that an average (i.e. global) stress
 1056 tensor is a meaningful quantity to characterize the
 1057 heap in spite of gravity, the Appendix B recalls
 1058 the expression of the latter tensor and the cor-
 1059 responding mean stress p in Equation B17. The
 1060 final states (e, p) of a large set of 400 heaps simu-
 1061 lated in the previous series CLP1, CLP4 together
 1062 with a forthcoming CLP5 (grouped under a CLPX
 1063 notation) are then compared in Figure 22 with the
 1064 CSL of the present granular material, previously
 1065 determined in [28] from DEM triaxial tests. The
 1066 latter were performed in quasi-static conditions
 1067 with a constant lateral stress in two directions and
 1068 an imposed a strain rate in the third direction.
 1069 Each of the 105 triaxial tests plotted on Figure
 1070 22 contained 7,500 clumps, which was shown to
 1071 be enough to constitute a REV for the study
 1072 of the material stress-strain behaviour. The crit-
 1073 ical state was observed to be attained when the

axial strain ϵ_{ax} reaches 0.6, i.e. both the devia- 1074
 toric stress and volumetric strain were unaffected 1075
 by further deformations. Any critical state quan- 1076
 tity is thus computed as an average of its value 1077
 over $\epsilon_{ax} \in [0.6, 0.8]$. It is to note that it was 1078
 shown in [28] to be more relevant to consider rat- 1079
 tlers (particles having at most 1 contact) as voids 1080
 when determining the CSL of a granular mate- 1081
 rial, to avoid an unphysical increase of the CSL 1082
 in the (e, p) plane for low p . This is especially 1083
 important here since body weights are the only 1084
 external forces present in the CLPX series, making 1085
 the average mean stress possibly quite low (≈ 100 1086
 Pa), depending on mass density. 1087

From the comparison in Figure 22, one can 1088
 first note that the mechanical states in the CLPX 1089
 series regroup around two different mean pres- 1090
 sures: $126 \pm 18 Pa$ and $1444 \pm 471 Pa$, in line with 1091
 the two different values used for the particle den- 1092
 sity throughout the CLPX series. Whatever the 1093
 mass density, the mean pressure in axisymmetric 1094

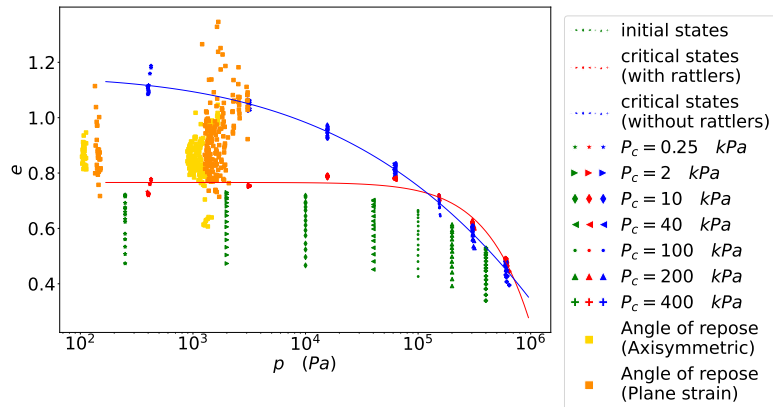


Fig. 22: Heaps' states after the collapse compared to the critical state line as determined in [28] from a large set of triaxial tests with different initial states in terms of void ratio and/or confining pressure P_c

1095 heaps is lower than the mean pressure in plane
 1096 strain heaps, and the dispersion in final void ratio
 1097 is smaller. Most importantly, the heap states are
 1098 clearly not consistent with the blue-colored (rat-
 1099 tlers excluded) CSL serving as reference, which
 1100 already suffices to exclude the assumption that a
 1101 heap of particles under gravity is at critical state.

1102 For completeness, the angle of repose of these
 1103 CLPX series is still furthermore directly compared
 1104 in Figure 23 with the critical state friction angle
 1105 ϕ_{crit} and the (porosity;mean stress)-dependent
 1106 peak friction angle ϕ_{peak} of the material, deter-
 1107 mined on the triaxial simulations from [28]. The
 1108 AOR is therein shown to be significantly differ-
 1109 ent (higher from approx. 10 degrees) than ϕ_{crit} .
 1110 It actually lies in the observed interval for ϕ_{peak} ,
 1111 even though both are observed to be essentially
 1112 different.

From the observations that the repose states
 are not consistent with the shear strength proper-
 ties of the granular material, neither the critical
 one nor the maximum one, the AOR is concluded
 to bear no constitutive nature. Interpreting the
 repose stress state σ_{ij}^{glob} with its extreme principal
 stresses $\sigma_1^{glob} \geq \sigma_3^{glob}$ in terms of a mobilized fric-
 tion angle ϕ_{mob} , given in Equation 36 using the
 soil mechanics sign convention:

$$\phi_{mob} = \arctan \left(\frac{\sigma_1^{glob} - \sigma_3^{glob}}{2\sqrt{\sigma_3^{glob}\sigma_1^{glob}}} \right) \quad (36)$$

1113 , no obvious correlation is actually found in
 1114 Figure 24, no matter the shape model, between
 1115 the mechanics of the heap, ϕ_{mob} , and its geom-
 1116 etry, α , which would have been mandatory for a
 1117 constitutive interpretation.

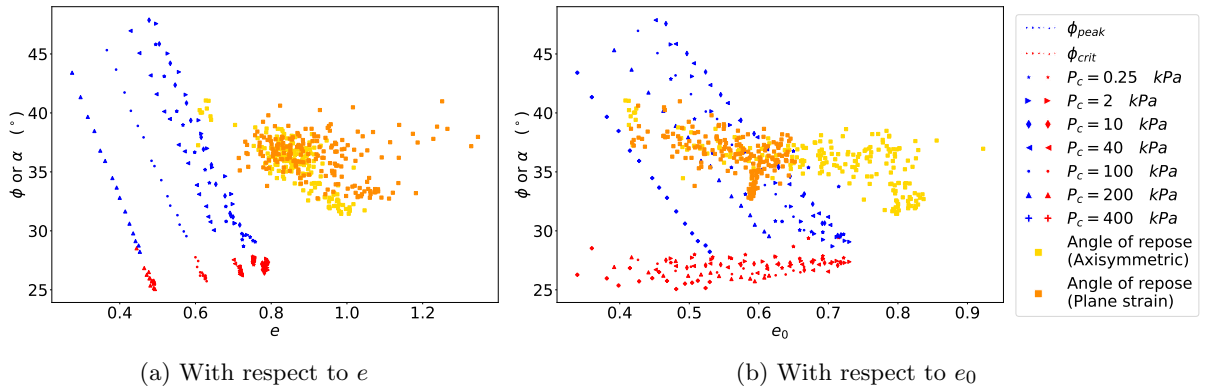


Fig. 23: Angle of repose α and triaxial properties, ϕ_{crit} and ϕ_{peak} , with respect to void ratio (current, e , or initial, e_0)

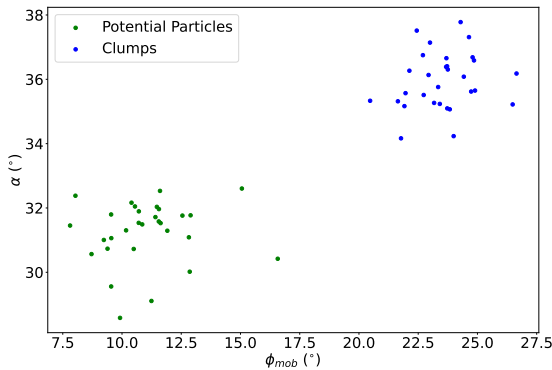


Fig. 24: Angle of repose α against mobilized friction angle ϕ_{mob} for heaps of the PP-CLP series.

4.5 Effect of the sample size on the angle of repose

Since the default number of particles in both configurations is low compared e.g. to the number of particles necessary to constitute a REV for the triaxial tests with rigid boundaries (7500 in [28, 29] for the same or another granular material), it is finally investigated to which extent the sample size can affect the present discussion, performing a last “CLP5” series that adopts the clump model and an evolving number of particles N_{part} (see

Table 12 for all parameters). Doing so, the dimensions of the container are homothetically modified according to $N_{part}^{1/3}$, which insures to keep similar geometries (consistent length ratios between every 3 axes) when the total volume $V \propto N_{part}$ increases.

Figure 25 shows the AOR values obtained in this CLP5 series, with error bars from the standard deviation computed on the ten simulations performed for each value of N_{part} . An exponential model is proposed to fit the data and provide an extrapolated value of α for an infinite number of particles:

$$\alpha_{model}(N_{part}) = a + be^{cN_{part}} \quad (37)$$

with a , b and c the three model parameters. Figure 25 (a) illustrates that the $N_{part} = 2,150$ case is the only one where the AOR values from both configurations are compatible with the idea of a common value. On Figure 25 (b) the horizontal

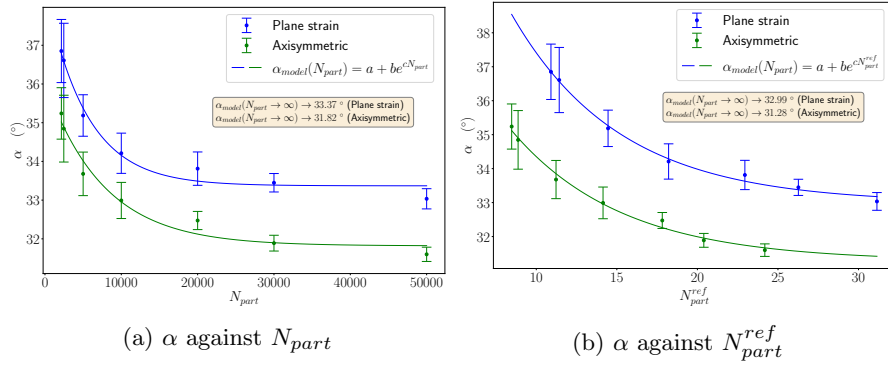


Fig. 25: Effect of the sample size on the angle of repose - CLP5 series

1147 axis represents N_{part}^{ref} , the number of particle along
 1148 one dimension of the base of the box:

$$N_{part}^{ref} = \left(\frac{N_{part}}{V_{box}} \right)^{\frac{1}{3}} L_{\eta} \quad (38)$$

1149 with $V_{box} \in \{V_{cyl}, V_{par}\}$ and $L_{\eta} \in \{R_{cyl}, L_{par}\}$.

1150 For bigger systems with a higher N_{part} a
 1151 clear difference appears, with a negligible stan-
 1152 dard deviation. According to the exponential
 1153 decay model, an asymptotic difference
 1154 between the two configurations would be 1.19°
 1155 which corresponds to approximately 3.59% of the
 1156 measurement in the plane strain configuration.

1157 The present dependency to N_{part} constitutes
 1158 a last argument against the constitutive nature
 1159 of the AOR, making fortuitous the near-similarity
 1160 of α initially observed between the two configura-
 1161 tions, in connection with the particular values of
 1162 N_{part} used in the reference experiments.

5 Conclusion

1163

1164 In the framework of a round-robin activity provid-
 1165 ing an experimental reference, the angle of repose
 1166 of a granular material has been studied with
 1167 DEM, adopting two distinct characterizations for
 1168 particle shape: concave clumps of spheres and
 1169 convex-simplified potential particles, with a quan-
 1170 tification of the morphological differences between
 1171 the two (and the experimental reference), in terms
 1172 e.g. of convexity and sphericity.

1173 A methodological discussion has then been
 1174 first proposed for generic angle of repose studies,
 1175 designing systematic measurement procedures of
 1176 the slope angle and of the void ratio of the heap,
 1177 the latter being a possible factor of influence onto
 1178 the former, as a fundamental property of granular
 1179 matter.

1180 Physically, a thorough analysis provided a
 1181 number of consistent observations that the AOR
 1182 measured on the considered devices does not

bear a constitutive nature but is instead process-dependent. In the comparison with experiments, while adopting a simpler measurement method of the AOR due to experimental limitations, the clump approach successfully predicted the AOR within a 8% tolerance. On the other hand, the potential particles underestimated to a greater extent the AOR, as expected due to their artificial convexity. Even though the material particles had a fairly high convexity value ($C = 0.954$), neglecting their local concavities brought down the AOR from $35.95 \pm 0.88^\circ$ to $31.26 \pm 0.95^\circ$.

It is interesting to note that both the clump and the potential particle shape descriptions share the same dimensions in terms of a minimal bounding box and thus the same flatness and elongation values, prompting the need for a systematic investigation of other particle-scale shape indices that would possibly affect the AOR.

Appendix A YADE implementations of visco-elasticity

With reference to the normal contact law in Equation 2 and for the clump approach (which use here the `Ip2_ViscElMat_ViscElMat_ViscElPhys` and `Law2_ScGeom_ViscElPhys_Basic` YADE classes), c_n is computed from a given normal

restitution coefficient e_n according to the mass-dependent expression of [30], recalled in Equation A1:

$$e_n = \begin{cases} \exp\left[-\frac{\beta}{\omega}\left(\pi - \arctan\frac{2\beta\omega}{\omega^2 - \beta^2}\right)\right] & \text{for } \beta < \frac{\omega_0}{\sqrt{2}} \\ \exp\left[-\frac{\beta}{\omega}\arctan\frac{2\beta\omega}{\omega^2 - \beta^2}\right] & \text{for } \beta \in \left[\frac{\omega_0}{\sqrt{2}}; \omega_0\right] \\ \exp\left[-\frac{\beta}{\Omega}\ln\frac{\beta + \Omega}{\beta - \Omega}\right] & \text{for } \beta > \omega_0 \end{cases} \quad (\text{A1})$$

where $\beta = \frac{c_n}{2m}$, $\omega_0 = \sqrt{\frac{K_n}{m}}$, $\omega = \sqrt{\omega_0^2 - \beta^2}$ and $\Omega = \sqrt{\beta^2 - \omega_0^2}$, with m being the harmonic-average particle mass and K_n the normal contact stiffness. Equation A1 is solved inside YADE using a small number of Newton-Raphson iterations to make the inverse calculation of c_n based on the desired value of e_n . A straightforward calculation of c_n for the linear contact model has been provided in Equation (B4) of [31] via curve-fitting of the exact solution of [30], which is not however employed here.

For the potential particles approach (through, e.g., `Ip2_FrictMat_FrictMat_KnKsPhys` and `Law2_SCG_KnKsPhys_KnKsLaw` classes), a viscous damping parameter β_n serves as input for deriving c_n , consistently with a desired e_n and [32] via Equation A2:

$$\beta_n = -\frac{\ln e_n}{\sqrt{\ln e_n^2 + \pi^2}} \quad (\text{A2})$$

1230 Then, the viscous damping coefficient is calcu-
1231 lated as in Equation A3:

$$c_n = 2\beta\sqrt{m \cdot K_n} \quad (\text{A3})$$

1232 Appendix B A global stress 1233 tensor 1234 accounting for 1235 gravity

1236 In order to evaluate the stress state of the heap,
1237 one has to compute the stress tensor from the con-
1238 tact forces of all the contacts. Moreover, gravity
1239 being present in the simulations and at the origin
1240 of the movement, gravitational forces should thus
1241 be accounted for. In this subsection:

- 1242 • \mathbb{S} is the set containing all particles,
- 1243 • \mathbb{C}^{ext} is the set containing all the contacts
1244 between particles and boundaries,
- 1245 • the upper-script $.^p$ specifies that the quantity is
1246 taken for a particle p ,
- 1247 • the upper-script $.^c$ specifies that the quantity is
1248 taken for a contact c ,
- 1249 • the sub-script $.,_{x_i}$ denotes the derivative with
1250 respect to x_i ,
- 1251 • the total volume of the heap is noted V and can
1252 be determined from the volumes of all tetrahe-
1253 drons V^{tet} given by the Delaunay triangulation

on particles centers (see previous section 3.3.1): 1254

$$V = \bigcup_{p \in \mathbb{S}} V^{tet}, \quad 1255$$

- the number of underline denotes the order of a 1256
tensor ($\underline{\cdot}$ for vectors and $\underline{\underline{\cdot}}$ for matrices), 1257
- the Kronecker symbol δ_{ij} and Einstein's nota- 1258
tion will be used, 1259
- classical sign convention for stress is adopted, 1260
where the traction vector $\underline{t} = \underline{\underline{\sigma}} \cdot \underline{n}$ applies onto 1261
the system for an outwards normal \underline{n} . 1262

The global stress tensor $\underline{\underline{\sigma}}^{glob}$ can be expressed 1263
according to the local stress tensor $\underline{\underline{\sigma}}$: 1264

$$\underline{\underline{\sigma}}^{glob} = \frac{1}{V} \int_V \underline{\underline{\sigma}} dV \quad (\text{B4})$$

One can compute $\underline{\underline{\sigma}}$ using the divergence of the 1265
third order tensor $\underline{\underline{\sigma}} \otimes \underline{x}$ (with \underline{x} the position of any 1266
point in V with respect to a given, even though 1267
arbitrary, origin): 1268

$$(\sigma_{ik}x_j)_{,k} = \sigma_{ik,k}x_j + \sigma_{ik}x_{j,k} \quad (\text{B5})$$

Since the measurement is made when the heap 1269
is under equilibrium, the following equation holds, 1270
denoting \underline{g} the gravitational acceleration and ρ the 1271
particle density: 1272

$$\sigma_{ij,j} = -\rho g_i \quad (\text{B6})$$

Moreover, $x_{j,k} = \delta_{jk}$, thus: 1273

$$\sigma_{ik}x_{j,k} = \sigma_{ij} \quad (\text{B7})$$

1274 By replacing Equation B6 and Equation B7 in
1275 Equation B5 one gets:

$$\sigma_{ij} = (\sigma_{ik}x_j)_{,k} + \rho g_i x_j \quad (\text{B8})$$

Equation B4 then gives:

$$\sigma_{ij}^{glob} = \frac{1}{V} \int_V \left((\sigma_{ik}x_j)_{,k} + \rho g_i x_j \right) dV \quad (\text{B9})$$

$$= \frac{1}{V} \sum_{p \in \mathbb{S}} \int_{V^p} \left((\sigma_{ik}x_j)_{,k} + \rho g_i x_j \right) dV \quad (\text{B10})$$

because $\sigma_{ij} \neq 0$ only on V^p

$$= \underbrace{\frac{1}{V} \sum_{p \in \mathbb{S}} \int_{V^p} (\sigma_{ik}x_j)_{,k} dV}_{\sigma_{ij}^C} + \underbrace{\frac{1}{V} \sum_{p \in \mathbb{S}} \int_{V^p} \rho g_i x_j dV}_{\sigma_{ij}^G} \quad (\text{B11})$$

1276 Particles having an homogeneous density, one
1277 furthermore has, with m^p and \underline{x}^p the mass and
1278 center of p :

$$\int_{V^p} \rho x_j dV = m^p x_j^p \quad (\text{B12})$$

1279 The part of $\underline{\underline{\sigma}}$ due to gravity (σ_{ij}^G) can thus be
1280 written:

$$\sigma_{ij}^G = \frac{1}{V} \sum_{p \in \mathbb{S}} m^p g_i x_j^p \quad (\text{B13})$$

1281 As for the part due to contacts (σ_{ij}^C), Green-
1282 Ostrogradski theorem gives:

$$\sigma_{ij}^C = \frac{1}{V} \sum_{p \in \mathbb{S}} \int_{\partial V^p} \sigma_{ik} x_j n_k dS \quad (\text{B14})$$

Considering the traction vector $\underline{t} = \underline{\underline{\sigma}} \cdot \underline{n}$, one
has:

$$\sigma_{ij}^C = \frac{1}{V} \sum_{p \in \mathbb{S}} \int_{\partial V^p} t_i x_j dS \quad (\text{B15})$$

The traction vector is not nil only on contact
points. Since the system is closed, contact forces
between particles cancel each other leaving only
forces coming from outside of V . As a conse-
quence, one can only consider the contact forces
between particles and walls. For these contacts f^c
denotes the contact force exerted by the wall on
the particle and x^c the contact point. One has:

$$\sigma_{ij}^C = \frac{1}{V} \sum_{c \in \mathbb{C}^{ext}} f_i^c x_j^c \quad (\text{B16})$$

Finally, the global stress tensor for a stable
heap of particles made of homogeneous particles
and subjected to gravity is:

$$\sigma_{ij}^{glob} = \frac{1}{V} \sum_{c \in \mathbb{C}^{ext}} f_i^c x_j^c + \frac{1}{V} \sum_{p \in V} m^p g_i x_j^p \quad (\text{B17})$$

The mean stress can then be computed as $p =$
 $\frac{\text{Tr}(\underline{\underline{\sigma}}^{glob})}{3}$.

Appendix C Influence of the wall velocity

In both configurations a wall holding the particles
moves in order to let them fall. The way parti-
cles fall depends on the velocity at which the wall

1303 moves, but once the heap is stabilized the mea-
 1304 surement of the AOR could be the same no matter
 1305 the velocity. This could allow the increase of the
 1306 wall velocity V_{wall} and thus the decrease of the
 1307 time cost. To know the influence of V_{wall} on the
 1308 AOR, a series of simulations, CLP3, is performed
 1309 with the clump model. Its parameters are given in
 1310 Table C1. For each value of the speed-up factor,
 1311 10 simulations are performed.

1312 Figure C1 shows the results of the CLP3 series.
 1313 The symbols correspond to the mean measure-
 1314 ment over the 10 simulations performed with the
 1315 same V_{wall} and the error bars represent the stan-
 1316 dard deviation. One can state that in the plane
 1317 strain configuration V_{wall} does not have an effect
 1318 on α . However, in the axisymmetric configura-
 1319 tion, α decreases sharply in the transition zone
 1320 $10 < V_{wall}/V_{wall}^{ref} < 100$. In the plane strain con-
 1321 figuration, $V_{wall}/V_{wall}^{ref} = 10,000$ can thus be used,
 1322 while one should restrict to $V_{wall}/V_{wall}^{ref} = 10$ in
 1323 the axisymmetric configuration. Table C2 gives a
 1324 summary of the value of V_{wall} used throughout all
 1325 AOR simulations in this paper.

1326 Data availability

1327 All YADE scripts used to perform the PP-CLP
 1328 series are available online at [https://forgemia.
 1329 inra.fr/sacha.duverger/aor_nc_aix](https://forgemia.inra.fr/sacha.duverger/aor_nc_aix).

Acknowledgements 1330

We thank the Japanese Geotechnical Society for
 1331 organizing the DEM round robin test that moti-
 1332 vated this study. The efforts of Dr Shuji Moriguchi
 1333 (Tohoku University) are in particular gratefully
 1334 acknowledged. We also acknowledge the support
 1335 from the French "Sud" region to the recent LS-
 1336 ENROC project with an acquisition of a server
 1337 machine that could accomodate the 980 simula-
 1338 tions presented herein. 1339

Compliance with Ethical 1340

Standards 1341

The authors have no competing interests to
 1342 declare that are relevant to the content of this
 1343 article. 1344

References 1345

- 1346 [1] Derek Geldart, EC Abdullah, A Hassanpour,
 1347 LC Nwoke, and IJCP Wouters. Character-
 1348 ization of powder flowability using measure-
 1349 ment of angle of repose. *China Particuology*,
 1350 4(3-4):104–107, 2006.
- 1351 [2] Hamzah M Beakawi Al-Hashemi and Omar
 1352 S Baghabra Al-Amoudi. A review on the
 1353 angle of repose of granular materials. *Powder
 1354 technology*, 330:397–417, 2018.
- 1355 [3] Pascale C Rousé. Comparison of methods
 1356 for the measurement of the angle of repose

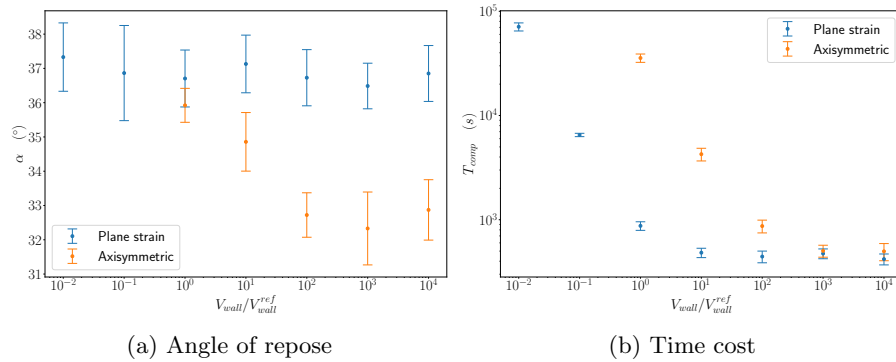


Fig. C1: Wall velocity influence on the angle of repose and on the time cost - CLP3

- 1357 of granular materials. *Geotechnical Testing*
 1358 *Journal*, 37(1):164–168, 2014.
- 1359 [4] Yukio Nakata, Shuji Moriguchi, Shin-
 1360 taro Kajiyama, Ryunosuke Kido, Naotaka
 1361 Kikkawa, Hidetaka Saomoto, Daiki Takano,
 1362 and Yosuke Higo. Experimental data of 3d
 1363 printed granular material for verification of
 1364 discrete element modeling simulation. *Soils*
 1365 *and Foundations*, 62(4):101178, 2022.
- 1366 [5] M. D. Bolton. The strength and dilatancy of
 1367 sands. *Géotechnique*, 36(1):65–78, 1986.
- 1368 [6] Michael Rackl and Kevin J. Hanley. A
 1369 methodical calibration procedure for discrete
 1370 element models. *Powder Technology*, 307:73–
 1371 83, 2017.
- 1372 [7] Thomas Roessler, Christian Richter, André
 1373 Katterfeld, and Frank Will. Development
 1374 of a standard calibration procedure for the
 1375 dem parameters of cohesionless bulk materi-
 1376 als – part i: Solving the problem of ambiguous
 1377 parameter combinations. *Powder Technology*,
 1378 343:803 – 812, 2019.
- [8] H.G. Matuttis, S. Luding, and H.J. Her- 1379
 rmann. Discrete element simulations of dense 1380
 packings and heaps made of spherical and 1381
 non-spherical particles. *Powder Technology*, 1382
 109(1):278–292, 2000. 1383
- [9] YC Zhou, BH Xu, AB Yu, and Paul Zulli. 1384
 Numerical investigation of the angle of repose 1385
 of monosized spheres. *Physical Review E*, 1386
 64(2):021301, 2001. 1387
- [10] Miki Y Matsuo, Daisuke Nishiura, and Hide 1388
 Sakaguchi. Geometric effect of angle of repose 1389
 revisited. *Granular Matter*, 16(4):441–447, 1390
 2014. 1391
- [11] Thorsten Pöschel and Volkhard Buchholtz. 1392
 Static friction phenomena in granular mate- 1393
 rials: Coulomb law versus particle geometry. 1394
Phys. Rev. Lett., 71:3963–3966, 1993. 1395
- [12] Hao Chen, Shiwei Zhao, and Xiaowen Zhou. 1396
 Dem investigation of angle of repose for 1397
 super-ellipsoidal particles. *Particuology*, 1398
 50:53–66, 2020. 1399
- [13] Nikola Topić, Jason AC Gallas, and Thorsten 1400

- 1401 Pöschel. Nonuniformities in the angle
1402 of repose and packing fraction of large
1403 heaps of particles. *Physical review letters*,
1404 109(12):128001, 2012.
- 1405 [14] Fathan Akbar, Elfi Yuliza, Nadya Amalia,
1406 Handika Dany Rahmayanti, and Mikrajuddin
1407 Abdullah. The slope of dry granular materials
1408 surface is generally curved. *Granular Matter*,
1409 24(69), 2022.
- 1410 [15] Hidetaka Saomoto, Naotaka Kikkawa, Shuji
1411 Moriguchi, Yukio Nakata, Masahide Otsubo,
1412 Vasileios Angelidakis, Yi Pik Cheng, Kevin
1413 Chew, Gabriele Chiaro, Jérôme Duriez,
1414 Sacha Duverger, Joaquín Irazábal González,
1415 Mingjing Jiang, Yohei Karasaki, Akiko Kono,
1416 Xintong Li, Zhuyuan Lin, Asen Liu, Sadegh
1417 Nadimi, Hitoshi Nakase, Daisuke Nishiura,
1418 Utsa Rashique, Hiroyuki Shimizu, Kumpei
1419 Tsuji, Takashi Watanabe, Xiaomin Xu, and
1420 Mourad Zeghal. Round robin test on angle
1421 of repose: Dem simulation results collected
1422 from 16 groups around the world. *Soils and
1423 Foundations*, 63(1):101272, 2023.
- 1424 [16] V. Smilauer et al. *Yade Documentation 3rd
1425 ed.* The Yade Project, 2021. [http://yade-](http://yade-dem.org/doc/)
1426 [dem.org/doc/](http://yade-dem.org/doc/).
- 1427 [17] Vasileios Angelidakis, Sadegh Nadimi,
1428 Masahide Otsubo, and Stefano Utili.
1429 CLUMP: A Code Library to generate Uni-
1430 versal Multi-sphere Particles. *SoftwareX*,
1431 15:100735, 2021.
- [18] Jean-Francois Ferrellec and Glenn R McDow- 1432
ell. A method to model realistic particle 1433
shape and inertia in DEM. *Granular Matter*, 1434
12(5):459–467, 2010. 1435
- [19] Guy Tinmouth Houlsby. Potential particles: 1436
a method for modelling non-circular parti- 1437
cles in DEM. *Computers and Geotechnics*, 1438
36(6):953 – 959, 2009. 1439
- [20] Chia Weng Boon, Guy Tinmouth Houlsby, 1440
and Stefano Utili. A new contact detec- 1441
tion algorithm for three-dimensional non- 1442
spherical particles. *Powder Technology*, 1443
248:94 – 102, 2013. Discrete Element Mod- 1444
elling. 1445
- [21] Reid Kawamoto, Edward Andò, Gioacchino 1446
Viggiani, and José E Andrade. Level set dis- 1447
crete element method for three-dimensional 1448
computations with triaxial case study. *Jour- 1449
nal of the Mechanics and Physics of Solids*, 1450
91:1–13, 2016. 1451
- [22] Jérôme Duriez and Cédric Galusinski. A 1452
level set-discrete element method in yade 1453
for numerical, micro-scale, geomechanics with 1454
refined grain shapes. *Computers & Geo- 1455
sciences*, 157:104936, 2021. 1456
- [23] Jérôme Duriez and Stéphane Bonelli. Pre- 1457
cision and computational costs of Level Set- 1458
Discrete Element Method (LS-DEM) with 1459
respect to DEM. *Computers and Geotechnics*, 1460
134:104033, 2021. 1461

- 1462 [24] Vasileios Angelidakis, Sadegh Nadimi, and
1463 Stefano Utili. SHape Analyser for Particle
1464 Engineering (SHAPE): Seamless characteri-
1465 sation and simplification of particle morphol-
1466 ogy from imaging data. *Computer Physics
1467 Communications*, 265:107983, 2021.
- 1468 [25] Hakon Wadell. Volume, shape, and round-
1469 ness of rock particles. *The Journal of Geology*,
1470 40(5):443–451, 1932.
- 1471 [26] Bruno Chareyre and Pascal Villard. Dynamic
1472 spar elements and discrete element methods
1473 in two dimensions for the modeling of soil-
1474 inclusion problems. *Journal of Engineering
1475 Mechanics*, 131(7):689–698, 2005.
- 1476 [27] Claudio Rocchini and Paolo Cignoni. Gener-
1477 ating random points in a tetrahedron. *Jour-
1478 nal of graphics Tools*, 5(4):9–12, 2000.
- 1479 [28] Sacha Duverger, Jérôme Duriez, Pierre
1480 Philippe, and Stéphane Bonelli. Rattlers’
1481 involvement for possibly looser critical states
1482 under higher mean stress. In *EPJ Web of
1483 Conferences*, volume 249, page 11002. EDP
1484 Sciences, 2021.
- 1485 [29] T. Mohamed, J. Duriez, G. Veylon, and
1486 L. Peyras. DEM models using direct and
1487 indirect shape descriptions for Toyoura sand
1488 along monotonous loading paths. *Computers
1489 and Geotechnics*, 142:104551, 2022.
- 1490 [30] Thomas Schwager and Thorsten Pöschel.
1491 Coefficient of restitution and linear-dashpot
model revisited. *Granular Matter*, 9(6):465–
469, 2007.
- [31] Colin Thornton, Sharen J Cummins, and
Paul W Cleary. An investigation of the
comparative behaviour of alternative con-
tact force models during inelastic collisions.
Powder technology, 233:30–46, 2013.
- [32] D Antypov and JA Elliott. On an analytical
solution for the damped hertzian spring. *EPL
(Europhysics Letters)*, 94(5):50004, 2011.

Table 11: Parameters used when investigating a possible influence of e_0 (CLP4 series, 200 simulations in total)

Configuration	N_{part}	ρ	e_0	Number of samples for each e_0
Plane strain	2, 150	10,000 kg/m^3	0.414 ± 0.010	10
			0.459 ± 0.009	
			0.480 ± 0.008	
			0.495 ± 0.006	
			0.504 ± 0.008	
			0.528 ± 0.006	
			0.536 ± 0.008	
			0.553 ± 0.010	
			0.567 ± 0.012	
			0.574 ± 0.007	
Axisymmetric	2, 468	10,000 kg/m^3	0.419 ± 0.006	10
			0.486 ± 0.006	
			0.525 ± 0.009	
			0.553 ± 0.006	
			0.577 ± 0.011	
			0.607 ± 0.018	
			0.626 ± 0.014	
			0.632 ± 0.010	
0.655 ± 0.012				
0.671 ± 0.016				

Configuration	N_{part}	ρ	e_0	Number of samples
Plane strain	2, 150 2, 468 5,000 10,000 20,000 30,000 50,000	10,000 kg/m^3	0.603 ± 0.010	10
			0.604 ± 0.009	
			0.596 ± 0.005	
			0.596 ± 0.003	
			0.594 ± 0.002	
			0.591 ± 0.003	
			0.588 ± 0.001	
			0.705 ± 0.011	
Axisymmetric	2, 150 2, 468 5,000 10,000 20,000 30,000 50,000	10,000 kg/m^3	0.693 ± 0.010	10
			0.729 ± 0.017	
			0.741 ± 0.006	
			0.758 ± 0.008	
			0.746 ± 0.016	
0.736 ± 0.004				

Table 12: Parameters of heap simulations investigating the influence of N_{part} (CLP5 series, 140 simulations in total)

Configuration	N_{part}	ρ	V_{wall}/V^{ref}	e_0	Number of samples
Plane strain	2,150	10,000 kg/m ³	10^i for $i \in [-2, 4] \cap \mathbf{N}$	0.603 ± 0.010	10
Axisymmetric	2,468		10^i for $i \in [0, 4] \cap \mathbf{N}$	0.693 ± 0.010	

Table C1: Parameters of heap simulations investigating V_{wall} influence (CLP3 series, 120 simulations in total)

Series	CLP1	CLP2	CLP4	CLP5	PP1	PP-CLP
V_{cyl}/V_{cyl}^{ref}	1	1	10	10	-	-
V_{par}/V_{par}^{ref}	1	1	10^4	10^4	10^3	10^3

Table C2: Wall velocity for all series of simulations